Comparison of flow characteristics behind squareback bluff-bodies with and without wheels

Citation for the original published paper (version of record):

Su, X., He, K., Xu, K. et al (2023). Comparison of flow characteristics behind squareback
bluff-bodies with and without wheels. Physics of Fluids, 35(3). http://dx.doi.org/10.1063/5.0138305

N.B. When citing this work, cite the original published paper.

(article starts on next page)

Comparison of flow characteristics behind squareback bluff-bodies with and without wheels

Xinchao Su (苏新超), Kan He (何侃), Kewei Xu (徐可为), et al.

View Online   Export Citation   CrossMark

ARTICLES YOU MAY BE INTERESTED IN

Effects of incoming free-stream turbulence on the flow dynamics of a square finite wall-mounted cylinder
Physics of Fluids 35, 025140 (2023); https://doi.org/10.1063/5.0137846
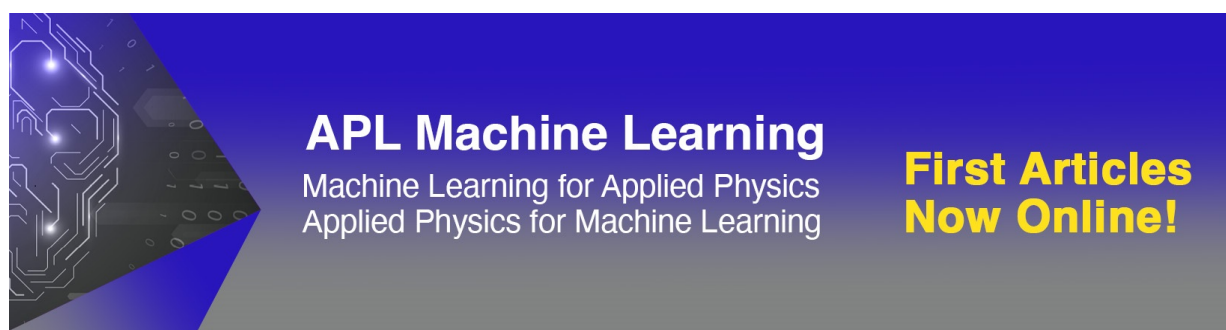
Temporal evolution of flow field structure for vehicles accelerating in evacuated tube transportation system
Physics of Fluids 35, 025117 (2023); https://doi.org/10.1063/5.0132163

A two-degree-of-freedom aeroelastic energy harvesting system with coupled vortex-induced-vibration and wake galloping mechanisms
Applied Physics Letters 122, 063901 (2023); https://doi.org/10.1063/5.0128616

AIP Publishing

Comparison of flow characteristics behind squareback bluff-bodies with and without wheels

Xinchao Su (苏新超),[1,2,3,4,a] (iD) Kan He (何侃),[4] (iD) Kewei Xu (徐可为),[4,b] (iD) Guangjun Gao (高广军),[1,2,3,b] (iD)
and Siniša Krajnović[4] (iD)

AFFILIATIONS

[1]Key Laboratory of Traffic Safety on the Track of Ministry of Education, School of Traffic & Transportation Engineering,
 Central South University, Changsha 410075, China
[2]Joint International Research Laboratory of Key Technology for Rail Traffic Safety, Central South University, Changsha 410075, China
[3]National & Local Joint Engineering Research Center of Safety Technology for Rail Vehicle, Changsha 410075, China
[4]Division of Fluid Dynamics, Department of Mechanics and Maritime Sciences, Chalmers University of Technology,
 SE-41296 Gothenburg, Sweden

[a]Electronic address: suxinchao@csu.edu.cn
[b]Authors to whom correspondence should be addressed: kewei@chalmers.se and gjgao@csu.edu.cn

ABSTRACT

The wake dynamics of two referenced variations of the squareback Windsor model with and without wheels is numerically studied by performing improved delayed detached eddy simulation. Numerical assessments are validated against publicly available experimental data. The focus of this study is on the wake states influenced by the wheels and the thick oncoming floor boundary layer. Results show that the addition of the wheels significantly changes the aerodynamic forces, the underbody flow, and the wake topology. The wake bi-stability is also enhanced with wheels in place due to the increased curvature of lateral shear layers in the near wake. However, the bi-stable behavior is largely suppressed when immersed in a thick boundary layer. These alterations depend on the degree of interaction between the wake recirculation and the bottom flow, and such degree is strongly affected by the underbody flow momentum. The evolution of low-order flow organizations and complementary spectral analysis highlight the differences in the coherent dynamics of the wake. The finding of this present work suggests that the wake bi-stability behind the squareback body can exist not only for a simplified geometry but also for a more realistic car with wheels in real-world upstream conditions.

Published under an exclusive license by AIP Publishing. https://doi.org/10.1063/5.0138305

I. INTRODUCTION

In the last decade, the targets for greenhouse gas emissions have become more stringent in response to climate change. Among different transport emissions, road travel accounts for the highest proportion (72% in Europe in 2019). Thus, most of the existing and planned actions are focused on road transport. For example, the new European regulation 2019/613 set CO_2 emission performance standards for new passenger cars and vans. As such, the growing constraints have motivated research activities to develop high-efficiency and clean vehicles. One of the active topics of interest is reducing aerodynamic drag to lower fuel consumption or extend the electric vehicle range.

Actually, automotive aerodynamics has long attracted the attention of industrial research particularly due to the energy crisis of the 1970s. Buchheim *et al.* (1981) summarized the semi-empirical optimization of basic bodies at that time and demonstrated quantitative effects of important shape parameters. Significant improvements have been made in correlating the individual drag sources to geometric changes, thanks to advances in specialized measuring techniques and computational fluid dynamics (CFD) methods since the 1990s. Hence, aerodynamic drag decreased rapidly by shape optimizations such as inclined front, cambered windshield, rounded A-pillars, boat-tailing C-pillars, covered wheel wells, smoothed underbody, etc., but soon came to its asymptotic value (Schuetz, 2015). Further improvement of the shape for drag reduction becomes increasingly difficult on the account of functional and stylistic limits. Consequently, a considerable literature has grown up regarding flow control strategies.

Prior to adopting flow control, fundamental studies have been made to advance our knowledge of the flow surrounding vehicles. It is known that most ground vehicles have a common feature of a blunt shape that provokes massively separated flow with complex wake dynamics. However, their shapes are many and diverse, and the variety makes it difficult to make a general guideline. The separated wake is the primary contributor to drag for passenger cars, so the rear-end design is very influential. Ahmed et al. (1984) experimentally investigated the effect of the rear slant angle on the dramatic increase in drag that is experienced by early hatchback cars. Afterward, the simplified scaled geometry of the Ahmed body is extensively used for fundamental investigations in pre-development and research (Le Good and Garry, 2004). Experimental (Zhang et al., 2015; Venning et al., 2017; and Liu et al., 2021) and numerical studies (Krajnović and Davidson, 2005; Rao et al., 2018) provided more insight into the three salient structures of the wake behind the body, i.e., a pair of counter-rotating longitudinal vortices developed from the C-pillars, a pair of recirculation regions, and a recirculation bubble over the slant. The interactions of these structures rely on the slant angle φ. Zhang et al. (2015) and Liu et al. (2021) provided detailed investigations on the high-drag regime ($12.5° < \varphi < 30°$) and the low-drag regime ($\varphi > 30°$), respectively. An abrupt fall in drag by 10% occurs at $\varphi = 30°$ owing to the separation shifted from the lower edge of the slant to the roof end. A bi-stable state has been observed for φ about 30° where the high- and low-drag regimes coexist (Kohri et al., 2014). In contrast, the drag is at its minimum at $\varphi = 12.5°$, and at even smaller angles, the flow pattern maintains highly similar to the squareback.

One conclusion drawn from the flow regimes is that to reduce aerodynamic drag, the separation at the slant top edge should be suppressed or promoted to avoid slant reattachment, resulting in a squareback-like flow. Passive flow control focused on the Ahmed body with 25° slanted surface using a rounded roof edge (Thacker et al., 2012) and impinging devices (Pujals et al., 2010; Krajnović, 2014). Such flow control strategies were able to delay rear slant separation, achieving 10% drag reduction. Other strategies used flaps (Beaudoin and Aider, 2008) and pulsed jets (Gilliéron and Kourta, 2013) to prevent or weaken the formation of longitudinal vortices, thus promoting the growth of the recirculation bubble resulting in a maximum drag reduction of 17.6% and 20%, respectively.

In recent years, more and more studies have been carried out on the squareback or squareback-like configuration since the squareback-like shapes (typical of station wagons, vans, and commercial vehicles) are very popular in today's automotive market for their convenient cargo storage or spaciousness. Unlike the slant end geometry consists of several interaction vortices, the topology behind the squareback is characterized by a very large recirculation region, which acts as a toroidal structure by the interaction of surrounding shear layers (Krajnović and Davidson, 2003). The wake dynamics of squareback Ahmed body is further revealed by Grandemange et al. (2013a). They found two distinctive scales presented in the wake: over long random timescale $T_l \sim 10^3 H/U_\infty$ of bi-stable behavior (where H is the body height and U_∞ is the free-stream velocity), the wake topology switches between two reflectional symmetry breaking states, while a short timescale $T_s \sim 5H/U_\infty$ corresponding to vortex shedding modes, the wake exhibits weak coherent oscillations in lateral and vertical directions. Moreover, a third dynamics, namely, pumping motion at higher Reynolds numbers using the same geometry was observed by Volpe

et al. (2015) with a normalized frequency of $St = fH/U_\infty = 0.08$ (roughly 1.5–2.5 times vortex shedding timescale). Historical studies over the past few decades on the flow control strategies mainly concentrated on the alteration or suppression of flow separation (Choi et al., 2014; Grandemange et al., 2015; Perry et al., 2016; Minelli et al., 2019; Xu et al., 2022, 2023; and Zhou et al., 2022). More recent attention has been focused on the suppression of the wake bi-stability, which is inspired by the 4%–9% drag reduction when the wake symmetric state is restored (Grandemange et al., 2014; Pavia et al., 2018; and Haffner et al., 2020). The flow control strategies such as deep base cavity (Evrard et al., 2016; Lucas et al., 2017), lateral slot (Li et al., 2016), pulsed jets (Barros et al., 2016), local base blowing (Plumejeau et al., 2019; Lorite-Díez et al., 2020; and Veerasamy et al., 2022), and feedback flaps (Brackston et al., 2016) have been successfully developed.

The aforementioned studies on ground vehicle aerodynamics were mostly performed on simplified geometries without wheels. Indeed, the basic shape is responsible for the largest contribution to the aerodynamic drag, contributing about 55% of overall drag (Schuetz, 2015). The wheels contributing to another large portion of aerodynamic drag are also of high interest. As reported in the experimental study by Wood et al. (2015), the drag increases by 24.4% when adding four stationary wheels to a generic sport utility vehicle with a 30° diffuser. The inclusion of wheels is also proven to significantly affect the wake balance. Huminic and Huminic (2017) investigated the effect of wheels on an Ahmed body with a 35° rear slant using Reynolds-averaged Navier–Stokes (RANS) simulations. Their flow visualizations show that the rear recirculation is squeezed between two streamwise vortices originating from the rear wheelhouses. Similarly, the flow field around an Ahmed body with a 25° rear slant and rotating wheels was provided by Gulyás et al. (2013) using particle image velocimetry (PIV). The complex vortex structures around the wheels of a production notchback car were depicted by Wäschle (2007) using wind tunnel measurements and RANS simulations. The rear wheels constrict the underbody flow, leading to a decrease in the efficiency of the rear diffuser. Aljure et al. (2018) studied the unsteady flow around the DrivAer fastback model using Large Eddy Simulation (LES). They visualized that the largest structures around the car are the jetting vortices created by the rotating wheels, which have a characteristic frequency of $St \approx 0.3$. The wheel–vehicle aerodynamic interaction was further investigated by Wang et al. (2020) via experiments on a test vehicle originating from the Asmo model. Their findings demonstrate that the balanced wake can be easily modified by different wheel states or tire modifications, especially at the rear axle. The wheels are regarded as underbody perturbations, and the relationship between wake balance and underbody flow momentum is roughly quantified. In addition, Wang et al. (2020) pointed out that the sensitivity of the wake balance configuration to wheel–vehicle interactions depends on vehicle geometry.

For a squareback geometry, the impact of wheels was included in extensive experimental campaigns conducted by Pavia (2019) and Varney (2020). They demonstrate that the wake of a squareback Windsor body shows an upwash dominance when wheels are added, leading to the removal of the bi-stable behavior and replacing it with a swinging motion of the rear recirculation (Pavia et al., 2020). However, a contradicted phenomenon was reported by Grandemange et al. (2013a), where the wake bi-stability was observed in the wind

tunnel experiments on a full-scale squareback Ahmed body with wheel spinners placed on a moving belt. No effort has been made to give a sound explanation for such contradicted results. Therefore, it is still uncertain whether the squareback model with wheels has a bi-stable wake or not. This motivates the current work to further study the flow physics of the wheel effect and to provide a physical explanation for such a conflict. In addition, only a few numerical studies are performed on this bi-stable wake due to its very long timescale. Hence, the differences in the unsteady three-dimensional wake behind squareback bluff-bodies with and without wheels remain to be compared in more detail. The numerical work presented in this paper further explores the wake bi-stable behavior and the coupling between the recirculating flow and the shear layers, which will help to examine whether existing flow control strategies applied to simplified geometries are also valid for more representative cars.

The remainder of this manuscript is organized as follows. The numerical setup including the mesh refinement study and accuracy validation is first presented in Sec. II. A comparison between the no-wheel and with-wheel cases with emphasis on the coherent wake dynamics is discussed in Sec. III. Concluding remarks follow in Sec. IV.

II. NUMERICAL DETAILS

### A. Geometries and boundary conditions

In this study, the two referenced variations of the squareback Windsor model, with wheels (wW) and without wheels (nW), are adopted from the ones experimentally tested by Varney et al. (2020). The model preserves the dimensions and aspect ratio of the Ahmed body but features a slanted front end that is more representative of passenger cars (Fig. 1). The body height of the model is $H = 0.289$ m. The width W and length L are 0.389 and 1.044 m, respectively. These dimensions correspond approximately to a 1:4 relationship with the real dimensions of a car. The four cylindrical supports with a diameter of 0.008 m are retained, and the ground clearance is set to $C = 0.05$ m to match the experiments. Detailed computer aided design (CAD) models included in the experimental dataset can be referred to Varney et al. (2020).

The computational domain for the simulations is present in Fig. 1. The inlet is set at $1.3L$ ahead of the model, and the outlet is located at $5L$ downstream, following the setup of Dalla Longa et al. (2019). The cross-section is set to $5W \times 4.6H$ to meet the experimental blockage ratio (4.7% and 4.4% depending on the model configuration). The coordinate system is denoted by x, y, and z for the streamwise, lateral, and vertical directions, respectively. Its origin is on the floor at the vertical centerline of the base. Conventional notations for the x, y, and z components of the instantaneous velocity field are denoted by u, v, and w, respectively. For any quantity χ, $\overline{\chi}$ represents the time-averaged value, while χ' is its fluctuating component. The superscript asterisk "*" is used to mark the normalized quantities. Reference values are the base height H and the free-stream velocity U_∞.

Since the incoming flow conditions have a strong influence on the unsteady wake characteristics (Kang et al., 2021; Aleyasin et al., 2021), two velocity inflow boundary conditions, i.e., uniform flow (U_1) and thick turbulent boundary layer flow (U_2), were investigated in this study. The 99% boundary layer thickness (δ_{99}) of the ground for Windsor body experiments is over 60 mm (Varney, 2020), and the corresponding ratio of the boundary layer thickness to ground clearance is $\delta_{99}/C = 1.2$. This ratio is twice that of typical car tests (Hucho et al., 1975) and about 2.4 times that of studies on Ahmed body (Grandemange et al., 2013a; Volpe et al., 2015). Thus, U_1 was used to be consistent with most studies conducted in the thin boundary layer (as summarized by Kang et al., 2021), while U_2 was used to compare with the experiments by Varney et al. (2020). The velocity distribution of U_2 was calculated based on the general behavior of the turbulent boundary layer (Cebeci, 2013), as shown in the inset of Fig. 1(a). The inlet turbulent intensity is set to 0.2%, same as the wind tunnel test section. Static pressure outlet boundary condition is applied at the outlet. The roof and sides of the domain are set as symmetry planes. Non-slip walls are specified on the floor and all surfaces of the model. Wheel rotation was not considered in current work as it produces marginal differences in either the time-averaged wake topology or unsteady behavior (Pavia, 2019; Rejniak and Gatto, 2021).

Two height-based Reynolds numbers were chosen, $Re = 5.78 \times 10^5$ and 0.96×10^5. The accuracy of numerical solution was assessed using experimental results of Varney et al. (2020) at the higher Re. The simulations on very long timescales required for bimodal detection were conducted at the lower Re to reduce computational effort.
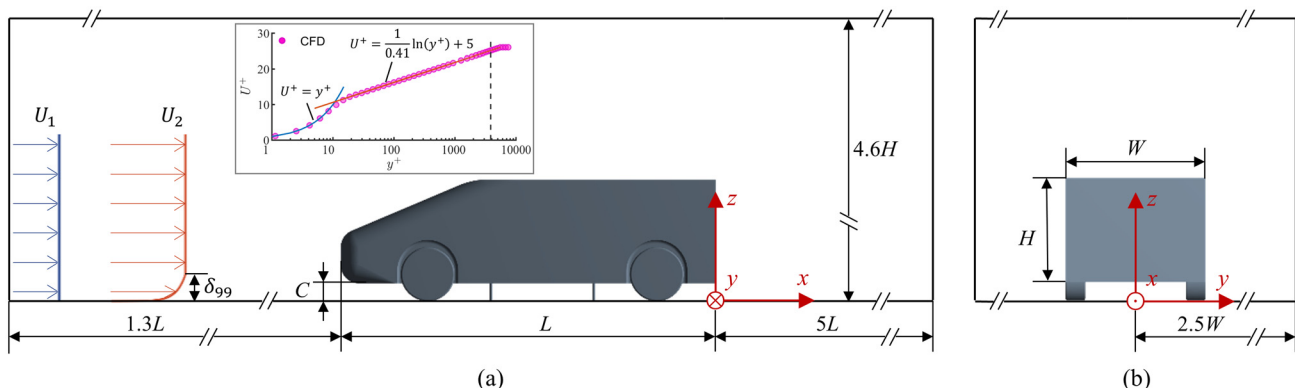
FIG. 1. Schematic of the numerical setup showing the employed nomenclature and investigated inflow conditions: (a) Side view and (b) back view. The parameters U^+ and y^+ in the inset of (a) are the longitudinal velocity and wall distance scaled based on the friction velocity (u_τ) and kinematic viscosity (ν), respectively, whereas the dashed line represents the location of the underbody.
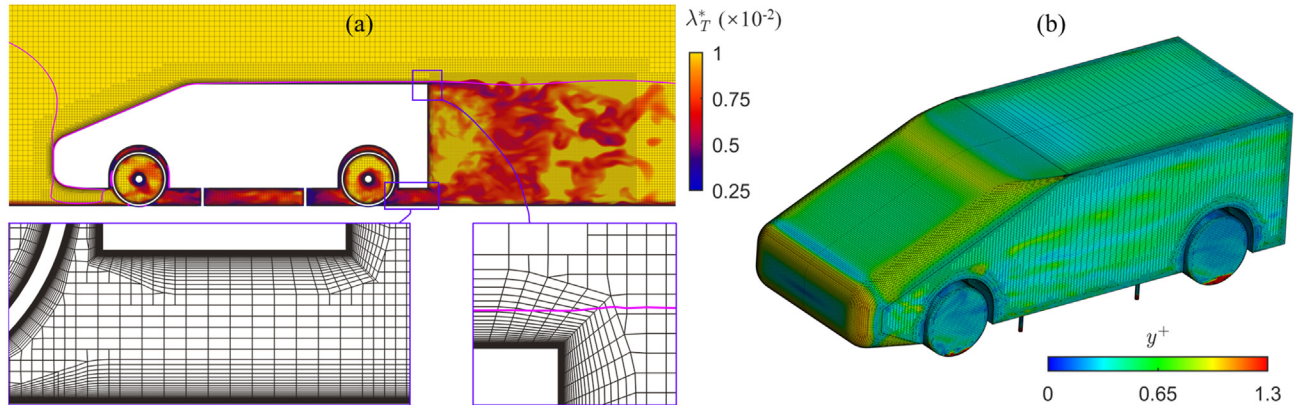
FIG. 2. Medium grid for wW cases at $Re = 0.96 \times 10^5$: (a) Mesh around the model in the plane $y^* = 0.58$, together with the contours of Taylor microscale λ_T^*. The magenta line represents the δ_{99} boundary layer. (b) Mesh on the body surface superimposed on y+ distribution.

Despite a small dependence of the global forces on the Reynolds number range (Varney, 2020), the bi-stability is independent of the Reynolds number in the turbulent regimes (Grandemange *et al.*, 2013a). Many previous studies (Grandemange *et al.*, 2013a, 2013b; Dalla Longa *et al.*, 2019; Fan *et al.*, 2020; Kang *et al.*, 2021; Hesse and Morgans, 2021; and He *et al.*, 2021a, 2022) on the bi-stability behavior around bluff-bodies were also conducted on the similar order of magnitude at the lower *Re*.

B. Numerical methods and mesh construction

The Improved Delayed Detached Eddy Simulation (IDDES) approach, which has been validated to capture bi-stability (Fan *et al.*, 2020; Kang *et al.*, 2021; and He *et al.*, 2021b), is used in the current study. As a hybrid modeling approach, the basic principle of IDDES is to use the RANS resolution in the boundary layer to save the near-wall resolving cost while retaining the fidelity of LES in the flow separated region. For the RANS portion, the shear stress transport (SST) *k-ω* model is employed here for its better performance in adverse pressure gradient flows and the free-stream independence (Gritskevich *et al.*, 2012). The continuity and momentum equations are discretized using the commercial finite volume solver STAR-CCM+. Specifically, the convective fluxes are discretized by the hybrid upwind scheme to blend the superiority of the second-order upwind scheme for RANS computations and the benefits of central differencing for LES. The diffusive fluxes are central-differenced with second-order accuracy. The transient term uses the implicit second-order accurate three-time level scheme. The integral conservation equations are solved in a sequential manner, and the pressure-velocity coupling algorithm employed is SIMPLE (semi-implicit method for pressure linked equations).

Hexahedron-dominant grids were constructed using the STAR-CCM+'s built-in trimmed meshing model. The symmetry of grids about the vertical center-plane is fulfilled by a mirror reflection of its half region to avoid introducing asymmetry in the flow. Mesh sensitivity testing was performed on three sets of grids (coarse, medium, and fine grids) for the wW model at $Re = 0.96 \times 10^5$. As the medium grid illustrated in Fig. 2(a), two levels of refinement regions are used to concentrate most of cells around critical regions of the body for higher accuracy. At the near wake, the isotropic cell size Δl_{wake}^+ measured in

the viscous length unit (ν/u_τ) is confined to 60 for better capturing the small-scale flow structures, as assessed using the instantaneous contour of Taylor microscale λ_T^* (the length scale separating the inertial range and the dissipation range). In the near-wall region, 28 prism layers are applied to body surfaces and the floor to solve the development of the boundary layer. The total thickness of the prism layers is thicker than the physical boundary layer to avoid the growth of the boundary layer being confined as seen from the enlarged view in Fig. 2(a). The wall normal resolution y^+ is less than 1.3. For the resolution in streamwise Δs^+ and spanwise Δl^+ directions, the maximum sizes are 240 and 60, respectively. The resolution around sharp edges Δl_{sharp}^+ is refined to 30. Those anisotropic surface cells and the distribution of y+ are displayed in Fig. 2(b). Coarse and fine grids use the same meshing strategy but with different grid spatial resolutions. More details regarding these grids are presented in Table I.

As for the temporal resolution, the time step Δt^* in convective time unit $t_c = H/U_\infty$ is 0.003 for $Re = 5.78 \times 10^5$ and 0.0075 for $Re = 0.96 \times 10^5$, giving the Courant–Friedrichs–Lewy (CFL) number lower than 1 in the main solution regions. Each simulation was first run for 75 t_c (about three flow passages through the domain) to achieve full development of the flow. Unsteady statistics were then obtained by sampling the flow field with a total duration (*T*) of 150 t_c for grid independence study, 300 t_c for computational validation, and 1350 t_c for wake bi-stability investigation.

C. Mesh sensitivity and validation

Mesh sensitivity assessments were conducted using the wW model at $Re = 0.96 \times 10^5$. The grid resolutions chosen for wW cases

TABLE I. Spatial resolution of grids.

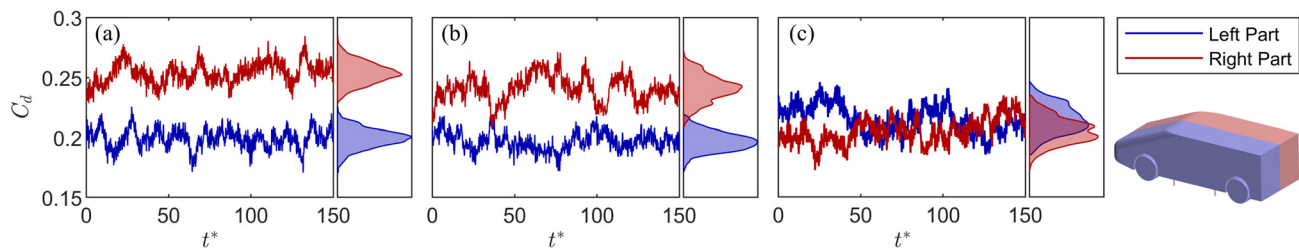| Re_H	Grid	Cell count[a]	y^+	Δs^+	Δl^+	Δl_{sharp}^+	Δl_{wake}^+
0.96×10^5	Fine	28.1×10^6	<1.3	<160	<40	<20	<40
	Medium	10.7×10^6	<1.3	<240	<60	<30	<60
	Coarse	5.7×10^6	<1.3	<320	<80	<40	<80
5.78×10^5	Medium	52.6×10^6n	<1.3	<240	<60	<30	<60

[a]Only the wheel cases are listed.

FIG. 3. Time history of drag coefficients and their associated PDFs for (a) fine grid, (b) medium grid, and (c) coarse grid.
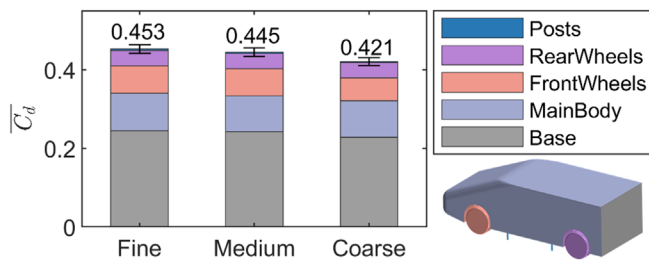

FIG. 4. Comparison of drag breakdown for different grid resolutions.

are expected to perform well in nW cases since the flow is more complicated in the former than in the latter. The uniform incoming flow (U_1) was applied to examine whether the long-time broken symmetry of the wake (discussed in more detail in Sec. III) could be resolved. Figure 3 presents the time history of aerodynamic drag coefficients C_d for the left and right halves of the model. Here, $C_d = F_d/(0.5\rho U_\infty^2 HW)$, where F_d is the aerodynamic drag and ρ is the air density. The reference area uses the area of the base excluding the wheels to have a fair comparison with the nW cases. For fine and medium grids, the right half suffers a markedly higher drag than the left half, while the two in the coarse grid are quite close, as highlighted by the probability density function (PDF). It indicates that the coarse grid fails to predict the flow asymmetry. A breakdown of contributions to the total drag is compared in Fig. 4. Note that the asymmetry of drag involved in bi-stability hardly affects the value of statistical mean drag as reported by Volpe *et al.* (2015).

The time-averaged drag coefficient $\overline{C_d}$ for each component predicted by the fine and medium grids is highly consistent, and the overall drag differs by less than 1.7%. Furthermore, shown in Fig. 5(a) are the time-averaged streamwise velocity profiles at $x^* = 0.05, 0.5, 1, 1.5$, and 2 in the vertical plane of symmetry. The velocity profiles from the fine and medium grid are quite similar, except for small deviations near the ground, while the coarse grid predicts the highest underbody velocity at $x^* = 0.05$, leading to gradual deviations downstream. The coarse grid has the longest recirculation region length (wake closure at $x^* \sim 1.5$), which is consistent with its minimum drag value. Shown in Fig. 6(a) is the time-averaged pressure coefficient $\overline{C_p}$ along the center-plane of the body. The pressure coefficients from the fine and medium grid are in good agreement everywhere, whereas the coarse grid mispredicts the $\overline{C_p}$ around the front roof and the lower part of the front end due to the overestimated separation. Considering that the medium and fine meshes produce very close results, the medium mesh was chosen as a good compromise between accuracy and computational effort.

Similarly, the accuracy of numerical simulations is verified on global quantities, velocity fields, and surface pressures. Force, pressure, and stereo PIV data at $Re = 7.7 \times 10^5$ and tomographic PIV data at $Re = 5.78 \times 10^5$ for the Windsor model are publicly available by Varney *et al.* (2020). Initially, the Reynolds number chosen for validation simulations is 5.78×10^5 for the comparison with the tomographic PIV data. However, given the fact that the overall flow is insensitive to a Re exceeding 4.2×10^5 (Varney, 2020), the stereo cross-plane data are finally chosen due to its higher spatial resolution. The incoming flow (U_2) with a boundary layer thickness of $1.3C$ was applied to reproduce the experimental condition. It should be noted
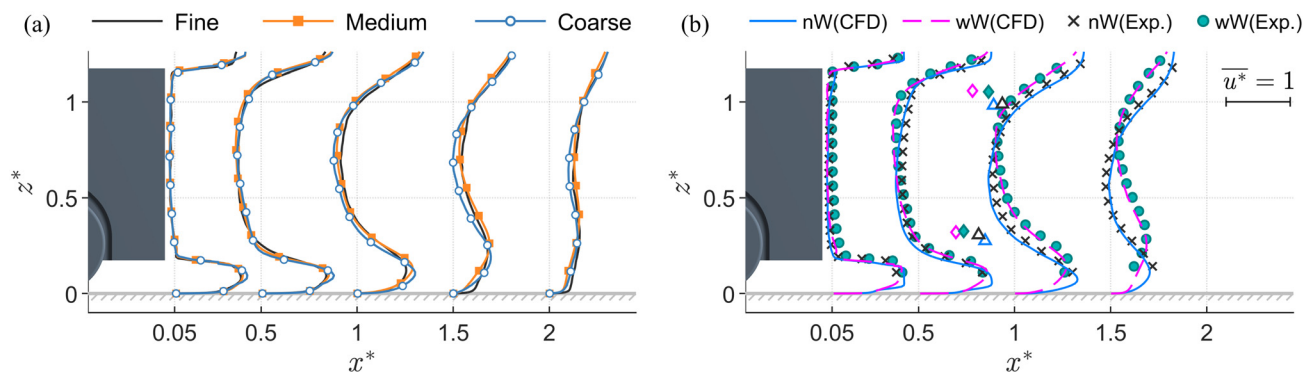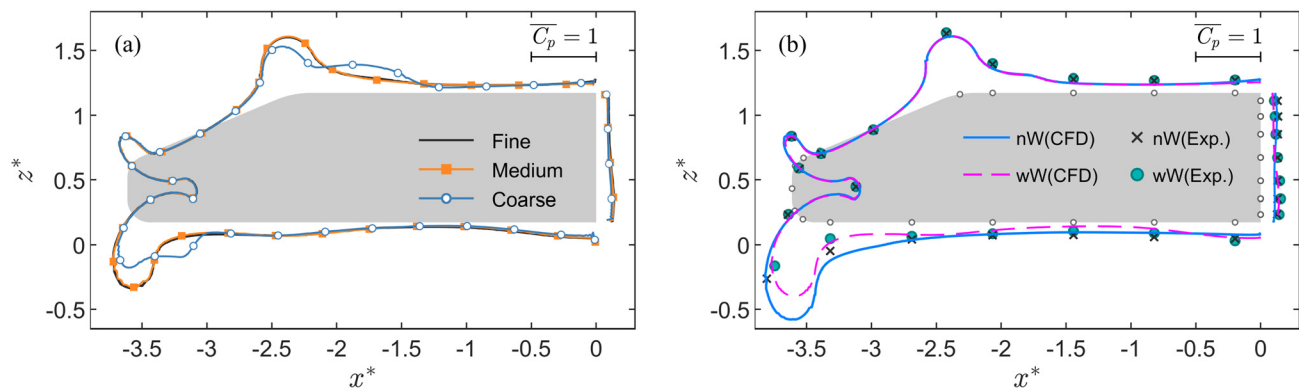

FIG. 5. Comparison of the mean streamwise velocity in the near wake at $y^* = 0$ (a) for different grids, and (b) between numerical results and experiments. The length for $\overline{u^*} = 1$ is indicated. The triangle and diamond symbols (same color as the corresponding profile) represent the location of vortex cores.

FIG. 6. Comparison of the mean pressure coefficient along the center-plane of the Windsor model (a) for different grids, and (b) between numerical results and experiments. The pressure coefficient is quantified by the distance normal to the body surface (positive for inward and negative for outward). The length for $\overline{C_p} = 1$ is indicated. The white circles in (b) denote the pressure taps location in the experiments, and the experimental pressure data here are the original data without correction.

that the Taylor microscale approximation is inversely proportional to the square root of the Reynolds number (Hesse and Morgans, 2021), which means that the resolution of the medium meshing strategy decreases at the higher Reynolds number.

The time-averaged global quantities are presented in Table II. For the drag coefficients $\overline{C_d}$, the numerical values for both the nW and wW cases are very close to the experimental results, with an error of less than 2% even considering the slight dependence on the Reynolds number. For the recirculation length $\overline{L_r^*}$ (defined by the maximum longitudinal length of the backflow region), the error is lower than 1% for the nW case, while the error is relatively larger for the wW case, but still less than 4%. For the base suction coefficient C_b (defined by integration of the pressure coefficient at the base as $C_b = -1/A \int C_p dA$, where A is the base surface), the mean values obtained in simulations are higher than that reported in experiments. A wide range of $\overline{C_b}$ for squareback Ahmed body has also been reported in the literature as summarized by Plumejeau *et al.* (2020). The strong variations observed are attributed to the underbody support obstructively and the ground clearance. However, here, it seems possible that the experimental results were overcorrected by blockage, e.g., the $\overline{C_b}$ of the wW case was corrected from 0.291 (Urquhart *et al.*, 2020) to 0.184 (the reference area here is the projected frontal area including the wheels). The contribution of the base suction to the total drag for the nW model in this study is about 84%, which is higher than the value reported by Varney (2020), but is consistent with that achieved from the experiment of Bao *et al.* (2022). More convincing evidence is that the center of the vortices in the wake fits well in the match between current simulations and the PIV data, as shown in Fig. 5(b).

TABLE II. Comparison of global quantities between simulations and experiments.

Re_H	Case	$\overline{C_d}$	$\overline{C_b}$	$\overline{L_r^*}$
5.78×10^5	nW (CFD)	0.281	0.235	1.52
	wW (CFD)	0.372	0.247	1.39
7.7×10^5	nW (Exp.)	0.280	0.177	1.51
	wW (Exp.)	0.370	0.193	1.34

Hence, the base suction obtained from current simulations can be considered reasonable. The velocity profiles of the simulations and experiments present in Fig. 5(b) are also in good agreement, and the slight mismatch can be attributed to the disagreements in the ground boundary layer leading to different underbody flows that further affect the wake downstream. Figure 6(b) compares the predicted pressure coefficients along the center-plane of the body with the uncorrected experimental results. The distribution is well reproduced for both the nW and wW cases, and the slight differences are likely to be related to blockage. In summary, all the above predictions from the numerical simulations agree well with the experimental results. Thus, the medium grid resolution is capable to accurately capture the flow for the squareback Windsor body, which is adopted in the current study.

III. RESULTS AND DISCUSSION

This section compares the wake characteristics of the nW and wW models, including the influence of approach flow conditions. First, the detection of wake bi-stability and corresponding wake topologies are presented in Sec. III A. Likely, reasons for the altered behavior behind the wake are then analyzed in Sec. III B. The impacts of wake dynamics modifications on aerodynamic forces and turbulent characteristics are outlined in Sec. III C. At last, the coherent dynamics of the wake together with temporal evolution is provided in Sec. III D.

Prior to the statistical analysis of flow characteristics, instantaneous flow structures around the two variations of Windsor model are presented in Fig. 7 to gain first insight into the influence of wheels. In the wheel case, the flow separates from the front wheels and wheelhouses forming large amounts of highly unsteady vortex structures, and large-scale hairpin vortices emanate from the redeveloping boundary layer near the side walls, whereas in the no-wheel case, only smaller scale eddies generated by the upstream struts and corner vortices rolling along the longitudinal edges are observed before the flow reaches the base. The lower vortices near the ground are stronger in terms of the increased velocity as compared to those in the wheel case. It is noteworthy that the horseshoe-like structure upstream the wW model results from shear motion instead of flow swirling. In both cases, massive vortex structures are generated and developed in the wake, resulting in complex interactions. The rich set of dynamics observed here is similar to the results reported in previous studies on
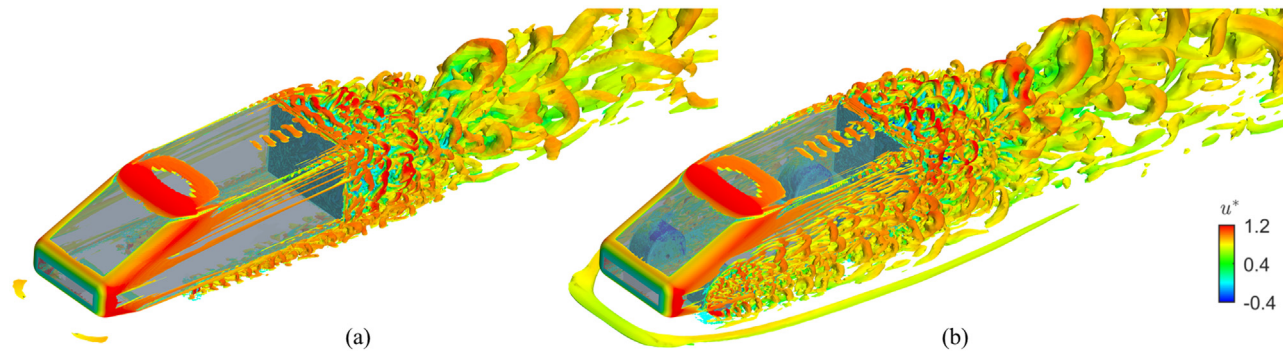
FIG. 7. Visualization of iso-surfaces of $\lambda_2^* = -0.5$ (Jeong and Hussain, 1995) colored by streamwise velocity for Windsor body (a) without wheels and (b) with wheels at $Re = 5.78 \times 10^5$.

squareback vehicle models (Lucas *et al.*, 2017; Dalla Longa *et al.*, 2019; Pavia *et al.*, 2020; Fan *et al.*, 2020; and Kang *et al.*, 2021).

In the rest of this work, three cases were studied for comparison: (i) the nW model in uniform inflow, (ii) the wW model in uniform inflow, and (iii) the wW model in thick boundary layer inflow (U_2). The U_2 inflow condition studied here, however, does not represent a realistic on-road condition (Kang *et al.*, 2021) and is used as a comparison case to the experimental findings of Pavia *et al.* (2020). For ease of reference, the three cases are denoted by cases nW, wW, and wW2. Their wake characteristics were examined at $Re = 0.96 \times 10^5$ for very long-time spans with the T^* more than 825.

A. Detection of wake bi-stability and corresponding wake topologies

Traces of bi-stable behavior are provided by the base suction coefficients C_b of the two vertical halves of the base. The base pressure gradient has been shown in previous research (Grandemange *et al.*, 2013b; Evrard *et al.*, 2016) to be an appropriate indicator for the wake asymmetry. Figure 8 shows the time history of C_b on each vertical half of the base (C_{bL} for the left side and C_{bR} for the right side). Long-time horizontal wake asymmetry can be distinctly identified in cases nW and wW for a total sampling time $T^* = 1350$. For case nW, the wake shifts its horizontal off-center position at t^* of 133, 1201, and 1308, representing a switch between the two reflectional symmetry breaking states. Rapid successive switches are ignored since the typical duration for a steady symmetry breaking mode suggested by Cadot (2016) should not be less than 100 t_c. The occurrence of such rapid switches reveals a high sensitivity of the wake (Haffner *et al.*, 2020), as the

asymmetric state stability is maintained by a weak interaction between underbody flow and the wake (Plumejeau *et al.*, 2020). In many previous experimental studies (Grandemange *et al.*, 2013a; Cadot *et al.*, 2015; Varney, 2020; Burton *et al.*, 2021; and He *et al.*, 2022), limited by high sampling intervals or the use of filtering to remove high-frequency sampling noise, certain short-time switches were usually omitted. As identified by Volpe *et al.* (2015) in their experiments on squareback Ahmed body, the calculated mean duration $\overline{\delta T^*}$ of the two stable positions decreased from 1092 to 421 when the resampling interval Δt_s^* was reduced from 92.7 to 4.6. In the LES study by Hesse and Morgans (2021), the maximum duration (δT^*) of one steady asymmetric state was 378 due to the even smaller time step. Consequently, the bi-stability timescale of case nW has the same order of magnitude as those reported in previous studies. Similarly, for case wW, bimodal events are recorded at t^* of 802, 919, 1036, and 1132. Note that less switching occurs in case wW, suggesting a more stable asymmetry state than in case nW. The same trend has also been identified by Bao *et al.* (2022) that the wheels (or the obstacles) have the ability to promote the appearance of bimodal dynamics in some cases. This will be explained in Sec. III D. Conversely, for case wW2, the two parts of C_b intersect frequently and show similar probability density distributions, unlike the two preferred positions for cases nW and wW (hence a shorter run time of 825 t_c for this case). As reported by Pavia (2019), the bi-stable mode is replaced by a swinging motion in the condition. This, however, does not necessarily imply the vanishing of the long-time instability, which can be evidently observed during t^* from 393 to 608 and in the experiments of Varney (2020).

Figure 9 shows the mean pressure distribution on the base for the three cases. The quite homogeneous distribution seen in the no-wheel
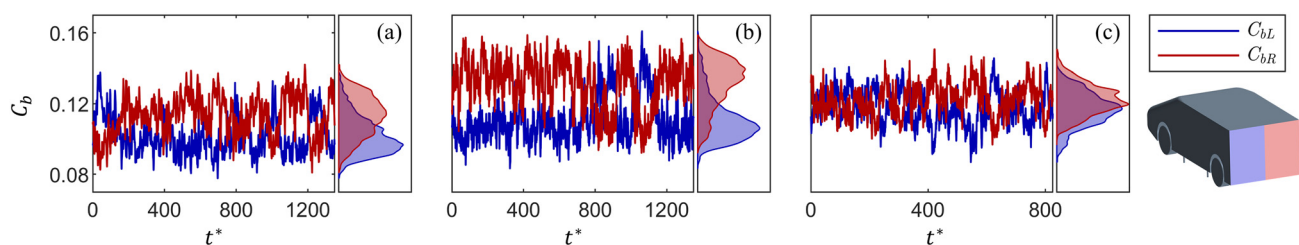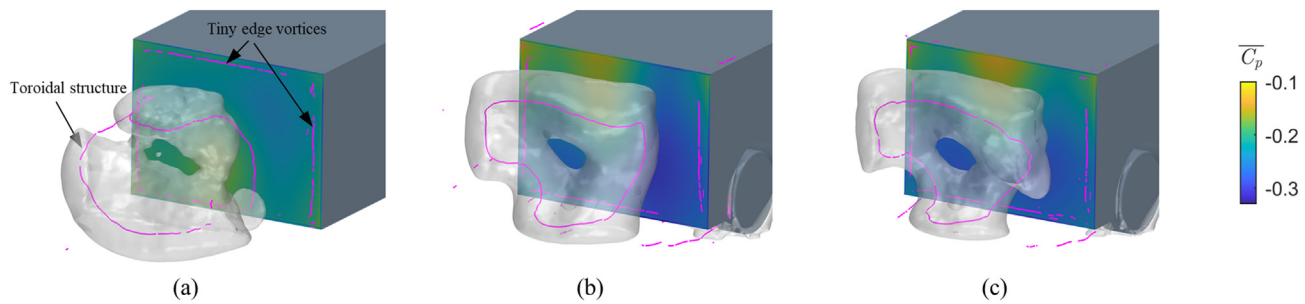

FIG. 8. Time history of base suction coefficients and their associated PDFs for (a) case nW, (b) case wW, and (c) case wW2.

FIG. 9. Time-averaged base pressure distribution and the toroidal structure visualized by iso-surface for (a) case nW at $\overline{C_p} = -0.31$, (b) case wW at $\overline{C_p} = -0.36$, and (c) case wW2 at $\overline{C_p} = -0.3\,45$. The pink curves represent the vortex cores.

model is replaced by a "U" shaped low-pressure region when wheels are equipped. This change is in agreement with the literature (Pavia, 2019; Varney, 2020; and Urquhart *et al.*, 2020). Consistent with the PDFs seen in Fig. 8, the pressure difference between the left and right parts of case wW is the largest, followed by case nW, while the pressure distribution in case wW2 is approximately laterally symmetric. As a result of the randomness of the long-time dynamics, the symmetry breaking position of case nW and wW happens to predominate on the right side (state R) in the current time window. Such statistical asymmetry induced by insufficient acquisition time is very common in the literature (Grandemange *et al.*, 2013a; Cadot *et al.*, 2015; Dalla Longa *et al.*, 2019; Pavia *et al.*, 2020; Plumejeau *et al.*, 2020; Kang *et al.*, 2021; Burton *et al.*, 2021; and Bao *et al.*, 2022) when bi-stability is involved. This is because achieving perfect statistical symmetry requires a recording time of over 60 times the long timescale $T_l \sim 10^3 H/U_\infty$ (Volpe *et al.*, 2015), which is time costly even for experiments. Fortunately, as proposed by Volpe *et al.* (2015), the perfect balance between the two wake states is not strictly necessary since the bi-stable fields are mutually symmetric, and it is possible to reconstruct the long-time symmetric field from the representation of a single state.

Figure 9 also shows the toroidal structure of the pressure coefficient behind the model for the three cases. A suitable iso-surface level was chosen for each of the three cases due to the different pressures in the near wake. The torus is determined through time-averaging the instantaneous coherent structures (Krajnović and Davidson, 2003) and has previously been reported in the wake of squareback models (Lucas *et al.*, 2017; Dalla Longa *et al.*, 2019; and Fan *et al.*, 2020). When wheels are added, the lower portion of the torus is narrower. The proximity of the vortex center (shown in pink) of large vortices is responsible for the region of lower pressure. For instance, influenced by the bi-stability phenomenon, the torus tilts toward the right side in cases nW and wW, which evidences the dominant state R corresponds to lower pressure at the right base. Likewise, in cases wW and wW2, the presence of wheels brings vortex cores closer to the base, resulting in a much lower base pressure than in case nW. In addition, tiny vortices are observed close to the four rear edges in case nW, while the upper-edge vortices are removed in cases wW and wW2.

To allow for a pertinent comparison of wake topology, conditional averaging based on the sign of $(C_{bR} - C_{bL})$ is performed to extract the preferred asymmetric states in cases nW and wW. For case wW2, where the wake manifests symmetry, the ensemble averaging is employed. In the following, the same symbol "⟨⟩" is used to denote quantities using the two averaging methods.

Figures 10(a) and 10(b) show the recirculation region in state R for cases nW and wW, respectively. The recirculation region for case wW is smaller than for case nW and extends upward, closer to the roof edge. The recirculation zone volume $\langle V^* \rangle$ for case wW is 0.64, which is 16% smaller than the 0.76 of case nW. The minor vortices near the roof edge are merged with the upward shifted reverse flow, consistent with that seen in Fig. 9. Both reverse flow zones are depressed on the right side corresponding to a larger recirculation bubble closer to the base as demonstrated by the in-plane streamlines at $z^* = 0.67$ (the base mid-height). The flow topology changes to symmetric about the lateral midplane for case wW2 [Fig. 10(c)], when the approaching flow has a thick boundary layer. The $\langle V^* \rangle$ in this case is 0.62, which is only 3% smaller than case wW in the state R. The mean location of recirculation bubbles in the mid-height plane is further compared in Fig. 10(d). As listed in Table III, when wheels are added to the model, the location of the right vortex core ($y^* > 0$) in the state R is almost unaffected, while the left vortex core shifts from $x^* = 0.981$ for case nW to $x^* = 0.706$ for case wW. In the lateral direction, the y-coordinate of the left vortex core in the state R of both case nW and wW is $y^* \sim -0.49$, roughly the same as that of the symmetric state (case wW2). In contrast, the right vortex core in the state R moves inward by nearly 30%. The distance between the left and right vortex cores in the streamwise direction of case nW is 0.636, 35% greater than the 0.413 of case wW. This may be linked to the growth in the level of unsteadiness seen in case nW.

B. Reasons for the altered behavior behind the wake

Figures 11(a)–11(c) show the distribution of the mean streamwise velocity, $\overline{u^*}$, projected on the cross-section beneath the base. A high $\overline{u^*}$ region is found under the three bodies. Notably, for case nW, this high $\overline{u^*}$ region extends laterally to a larger area on both sides. However, for wW and wW2, the high $\overline{u^*}$ region is confined to the center area separating the rear wheels. The normalized underbody volumetric flow rate is quantified by integration of $\overline{u^*}$ out of the underbody, i.e., $\overline{Q} = -1/A_1 \int \overline{u^*} dA_1$. The area A_1 is indicated by the dashed box in Fig. 11(a). The increased underbody blockage from the wheels reduces underbody flow rate from 0.885 in case nW to 0.694 in case wW (i.e., by almost 22%). The rate in case wW2 is further reduced by 8% over case wW due to the thicker ground boundary layer. To better quantify the exit flow, the $\overline{u^*}$ distribution along a lateral line through the middle height of the underbody gap is then displayed in Fig. 11(d). It is found that the minimum velocity locates just
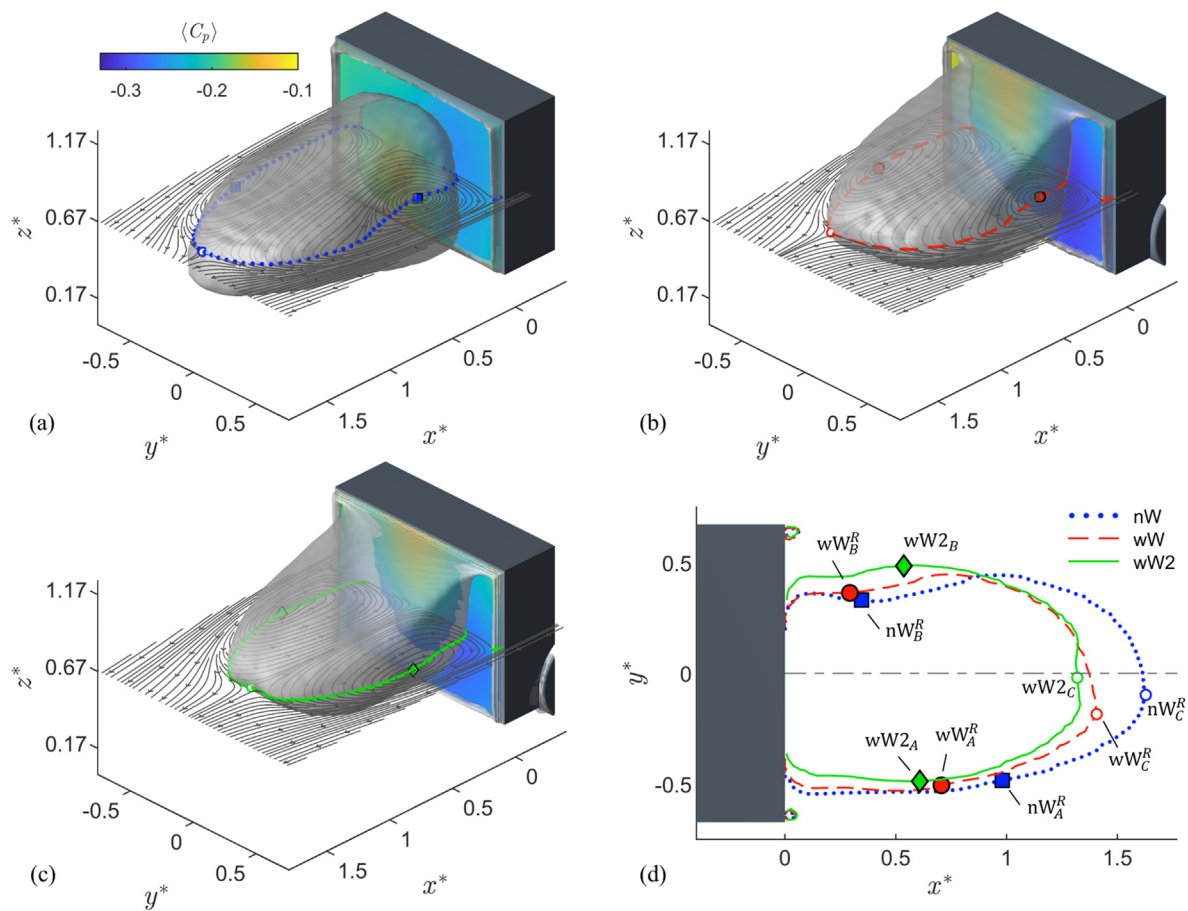
FIG. 10. Conditional or ensemble-averaged base pressure distribution and recirculation region (defined as the iso-contour $\langle u^* \rangle = 0$) together with the in-plane streamlines at $z^* = 0.67$ for (a) case nW, (b) case wW, and (c) case wW2. (d) Comparison of the location of vortex centers and saddle points in the plane $z^* = 0.67$ for the three cases.
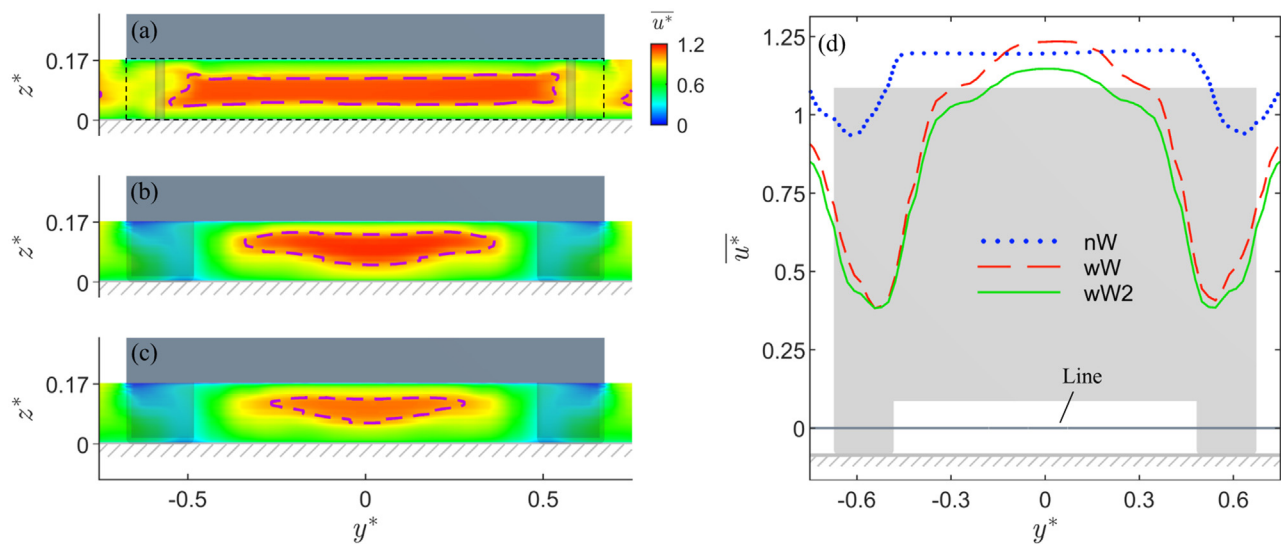
downstream of the cylindrical supports or the wheels with $0.93\,U_\infty$ for case nW and $0.38\,U_\infty$ for cases wW and wW2. The considerable momentum deficit downstream of the wheels is associated with the contraction at the lower part of the wake torus as seen in Fig. 9. More importantly, due to the jet-like effect, the maximum underbody flow velocity saturates to $1.20\,U_\infty$ between $-0.46 < y^* < 0.46$ for case nW. Unlike the velocity plateau present in case nW, the underbody flow velocities in cases wW and wW2 show a broad spike with maximum values of $1.23\,U_\infty$ and $1.15\,U_\infty$, respectively.

The effect of underbody flow on mean flow topology in lateral midplane $y^* = 0$ is presented in Fig. 12. A pair of recirculation bubbles, V_t and V_b, are observed behind the three models, which manifest

TABLE III. Location of the center of the vortices and the saddle points in the plane $z^* = 0.67$.

|	nW_A^R	nW_B^R	wW_A^R	wW_B^R	$wW2_A$	$wW2_B$	nW_C^R	wW_C^R	$wW2_C$
x^*	0.98	0.35	0.71	0.29	0.61	0.54	1.63	1.41	1.32
y^*	-0.48	0.33	-0.51	0.36	-0.49	0.49	-0.10	-0.19	-0.02

the cross-section of the toroidal structure observed in Fig. 9. For case nW [Fig. 12(a)], the top bubble V_t is slightly larger than the bottom one V_b, and the saddle point (marked as white dot) is located closer to the lower edge. For case wW [Fig. 12(b)], on the contrary, bubble V_b is much bigger in size, shifting the saddle point closer to the upper edge. For case wW2 [Fig. 12(c)], the saddle point rises to an even higher position. Such a switch from a downwash dominated wake to an upwash dominated wake is also reported in Grandemange *et al.* (2013b) when the ground clearance is decreased for the squareback Ahmed body. The distinct behaviors are a result of the competition between the downwash flow from the top and the upwash flow from the underbody. The underbody flow in case nW has the highest momentum, keeping it advected close to the ground, as depicted by the gray iso-contour $\overline{u^*} = 0.8$. However, the near-ground flow undergoes a noticeable upward deflection near $x^* = 1$ in cases wW and wW2 due to the reduced underbody flow rate. The raised upward entrainment shortens the recirculation length $\overline{L_r^*}$ by roughly 17%. Furthermore, the base impingement point (indicated by white square) moves toward the top trailing edge as the saddle point does, allowing for the pressure recovery on the upper portion of the base, forming the "U" shaped pressure distribution.

FIG. 11. The underbody flow velocity field beneath the base at $x^* = 0$ for (a) case nW, (b) case wW, and (c) case wW2. The magenta dashed lines indicate the iso-contour $\overline{u^*} = 1$. (d) Velocity profiles extracted from the line at vertical location $z = 0.5C$ in the base plane.
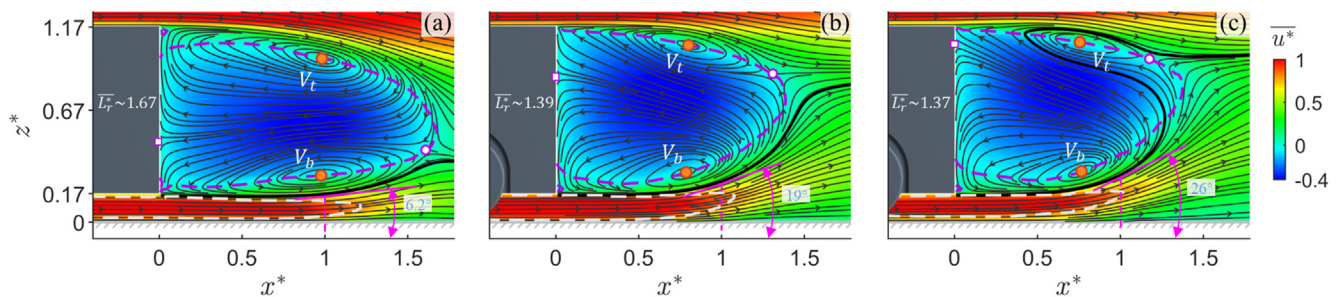

FIG. 12. Time-averaged streamwise velocity with two iso-value lines in symmetry plane $y^* = 0$ for (a) case nW, (b) case wW, and (c) case wW2. The magenta and gray iso-lines denote the contour levels of $\overline{u^*} = 0$ and 0.8, respectively. The bold streamline passing through points (0, 0, and 0.9C) highlights the underflow behavior for each case.

The bold streamline in Fig. 12 passing through points (0, 0, and 0.9C) highlights the underflow behavior for each case. In case nW, the underbody flow does not appear to recirculate and mix with the back-flow region. In case wW, the interaction between the underbody flow and the wake remains weak. In case wW2, however, the underbody flow is entrained to the top bubble, and the strong interaction is deemed to be responsible for the disappearance of bi-stability. Note the underbody flow rate in case wW2 is only 8% less than in case wW, but the inclination angle of the bottom flow (measured by the tangent to the bold streamline at $x^* = 1$) increases from 19° to 26°. This emphasizes the high sensitivity of bi-stability to upstream perturbations (Grandemange *et al.*, 2013b; Plumejeau *et al.*, 2020; and Bao *et al.*, 2022).

C. Impacts on aerodynamic forces and turbulent characteristics

Shown in Fig. 13 is the comparison of the time-averaged drag coefficients for each component in the three cases. With the wheels in place, the total drag for case wW shows an increase in 47% over

case nW. In detail, the contribution to the drag rise is 23% for the front wheels, 13% for the rear wheels, and 9% for the base. The remaining smaller increase in total drag is due to the main body having less suction around the lower front curvature surface as seen in Fig. 6(b). Case wW2 slightly reduces the overall drag by 6% compared to case wW, arguably owing to the weakened impingement effect of the incoming flow in the thick boundary layer condition.
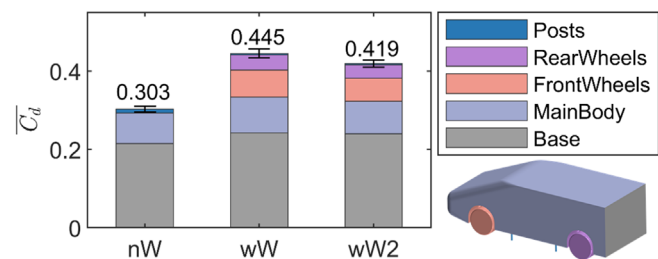

FIG. 13. Comparison of drag breakdown for different cases.

The characteristic of side force is vital to vehicle directional stability. Bi-stability, however, has been reported to induce variations in side force (Grandemange et al., 2013a; Plumejeau et al., 2020). Figure 14(a) presents the time history of the side force coefficient signals for the three cases. Indeed, the side forces for the asymmetric states in cases nW and wW are apparently shifted from zero. The mean side force coefficient of state R is $\langle C_y \rangle = 0.017 \pm 0.009$ in case nW and 0.024 ± 0.015 in case wW, indicating that the wheels increase both the mean and standard deviation of the side force. For case wW2, the mean side force coefficient is 0.003 ± 0.016. The very close standard deviations of cases wW and wW2 suggest that the fluctuation of the side force in the preferred state is insensitive to the incoming boundary layer. A spectral analysis of these signals reveals peaks at $St_H = 0.138$ for case nW, 0.122 and 0.635 for case wW, and 0.130 and 0.594 for case wW2 as seen in Fig. 14(b). Here, $St_H = fH/U_\infty$ is the non-dimensional frequency. The low frequency dynamics at $St_H \sim 0.13$ is associated with the lateral vortex shedding in the near wake. This result matches the experiments performed by Pavia et al. (2017) for the same geometry and is also documented in the literature for square-back Ahmed body (Grandemange et al., 2013a; Volpe et al., 2015; Lorite-Díez et al., 2020; Plumejeau et al., 2020; and Fan et al., 2020). Note that this low frequency is slightly smaller in case wW than in case nW, implying a weaker interaction of the lateral shear layer as a result of progressive flow separation stemming from front wheels as depicted in Fig. 7. A larger oscillation frequency around 0.6 is also observed in both wheel cases, expected to be the result of active vortex

shedding caused by wheels and wheelhouses. For cases nW and wW, the -2 power law captured at very low frequencies is consistent with previous research (Grandemange et al., 2013a; Volpe et al., 2015; Pavia et al., 2017; and Fan et al., 2020), confirming the existence of the bi-stable mode. As pointed out by Volpe et al. (2015), the vortex shedding mode is independent of the bi-stable behavior as the latter affects only very low frequency content. The asymmetric distribution of surface pressure in-state R for cases nW and wW presented in Fig. 14(c) is also associated with side forces. The apparent difference of pressure starts at point c, the middle of the rounded front edges for case nW, whereas such pressure difference appears more downstream for case wW from point d to e, the area above the front wheels. In contrast, the region of pressure asymmetry identified on the rear side of the body is essentially the same in both cases (from point f to g, $-1.2 < x^* < 0$), slightly larger than the corresponding region on squareback Ahmed body (Grandemange et al., 2013a). For case wW2, the surface pressures on both sides counterbalance each other on average.

The wheels modify the natural wake equilibrium in the vertical direction and thereby directly impact the turbulent statistical characteristics. A detailed examination of the Reynolds stresses in different planes is present in Fig. 15. In cases wW and wW2, the reduced momentum flow out of the underbody into the wake reduces Reynolds stresses in the bottom shear layer and considerably enhances the upper shear layer as seen in the plane $y^* = 0$ and $x^* = 1$. The bottom region of $\langle u'^* w'^* \rangle$ shows a strong upwash effect, and its peak is obviously influenced by the approaching flow. Instead, in case nW, the
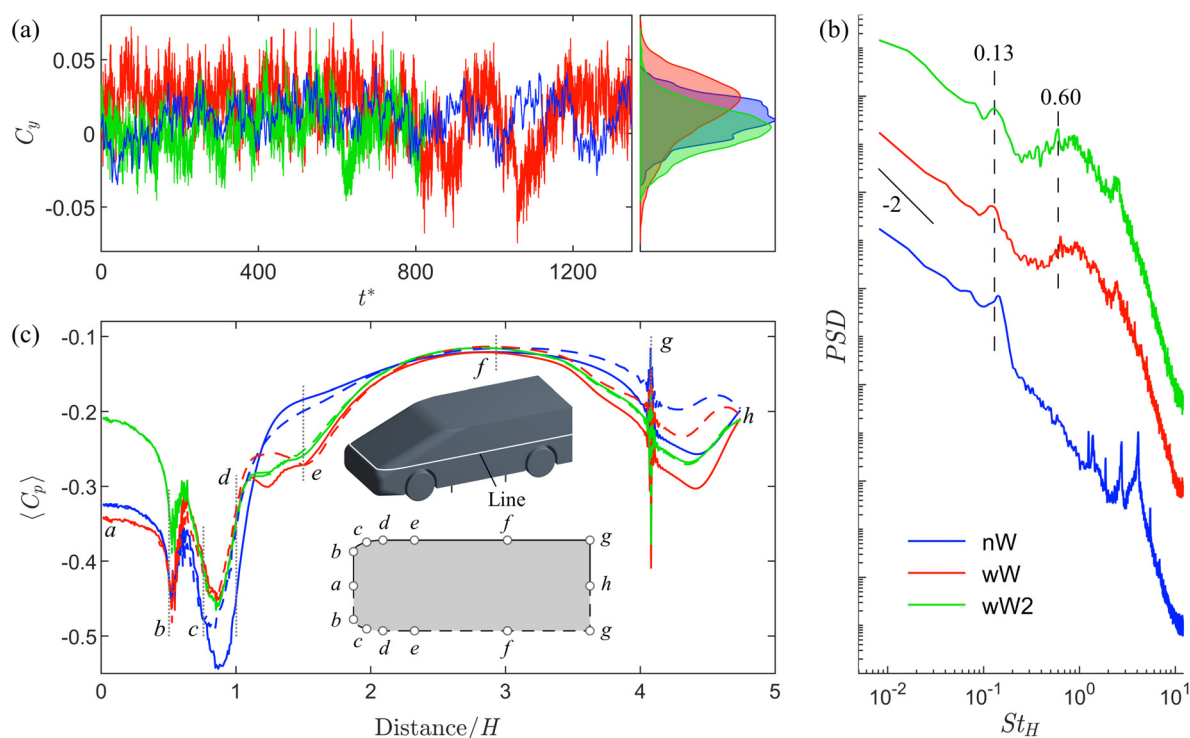
FIG. 14. Time history (a) and power spectra density (PSD) (b) of the side force coefficient signals. The curves in (b) have been vertically shifted to easily identify the peak frequencies. (c) Surface pressure distribution along the line at $z^* = 0.67$. The surface pressure on the left and right part of the model is indicated by dashed and solid lines, respectively.
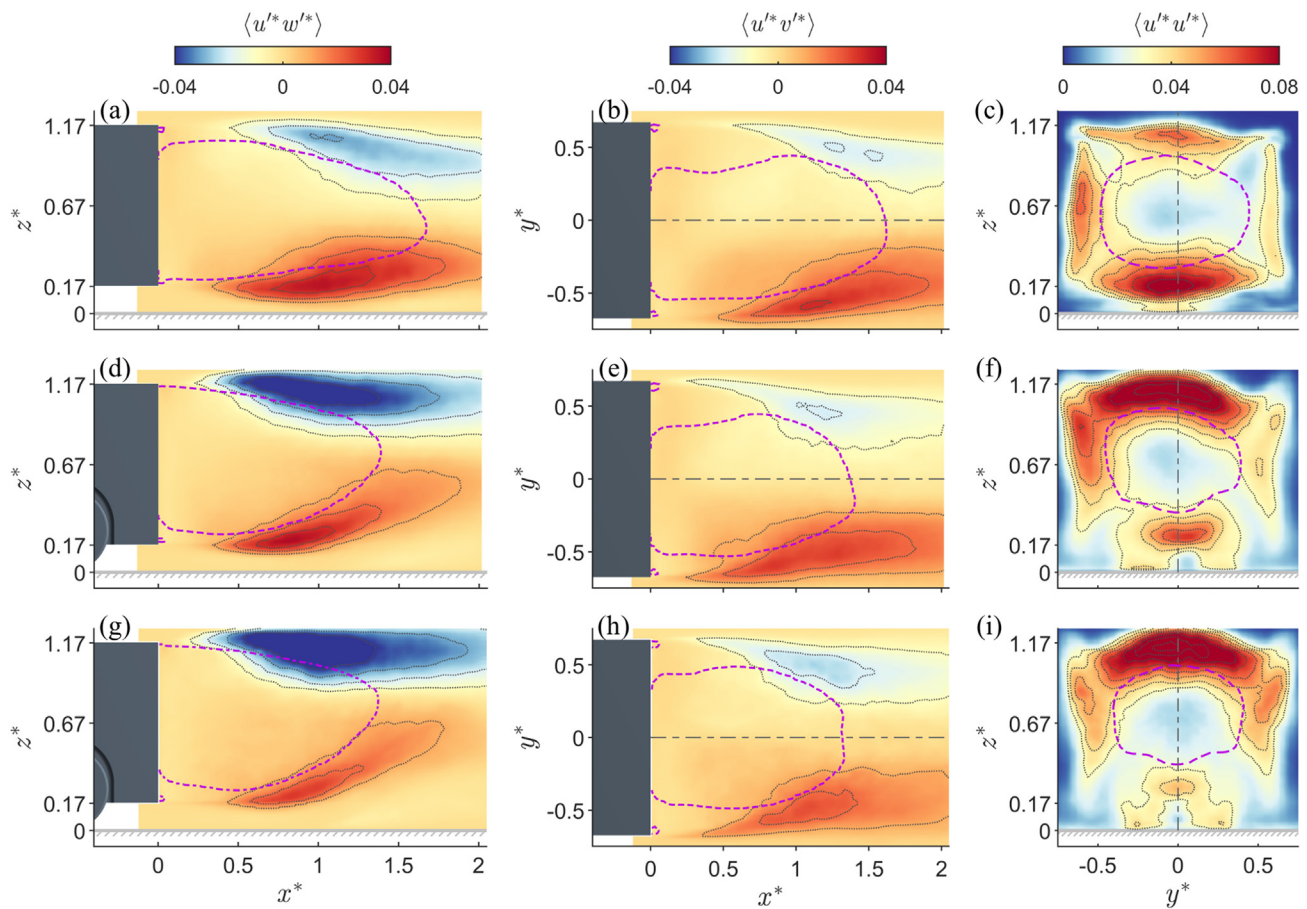
FIG. 15. Contours of the Reynolds stresses in the plane $y^* = 0$ [(a), (d), and (g)], $z^* = 0.67$ [(b), (e), and (h)], and $x^* = 1$ [(c), (f), and (i)] for case nW (a)–(c), case wW (d)–(f), and case wW2 (g)–(i). Contour intervals are 0.01. The magenta dashed lines are the iso-contour $\langle u^* \rangle = 0$.

top shear layer is slightly deflected toward the floor with a clearly smaller region of elevated Reynolds stresses compared to the lower shear layer. For lateral shear layers, Reynolds stresses are concentrated on the left side ($y^* < 0$) of the wake in the state R for cases nW and wW as shown in the plane $z^* = 0.67$ and $x^* = 1$. The enhanced turbulent fluctuations at the left side are related to a vigorous vortex shedding, while the damping of Reynolds stresses at the right side is associated with a quite static behavior of the larger bubble. The different activities will be further elucidated in Subsection III D.

Figure 16 provides a more quantitative comparison of the flow states through turbulence kinetic energy $\langle k^* \rangle$ in four lines bounding the wake. On the bottom line, $\langle k^* \rangle$ is damped at maximum by ~12% in case wW and by ~30% in case wW2 relative to case nW. In contrast, $\langle k^* \rangle$ along the top line is consistently higher in cases wW and wW2, with increases of up to 64%. The significant modifications in $\langle k^* \rangle$ for the lower and upper shear layers are related to the momentum of the underbody flow as discussed previously. Similar to the distribution of shear stresses, the maximum value of $\langle k^* \rangle$ on the left line is
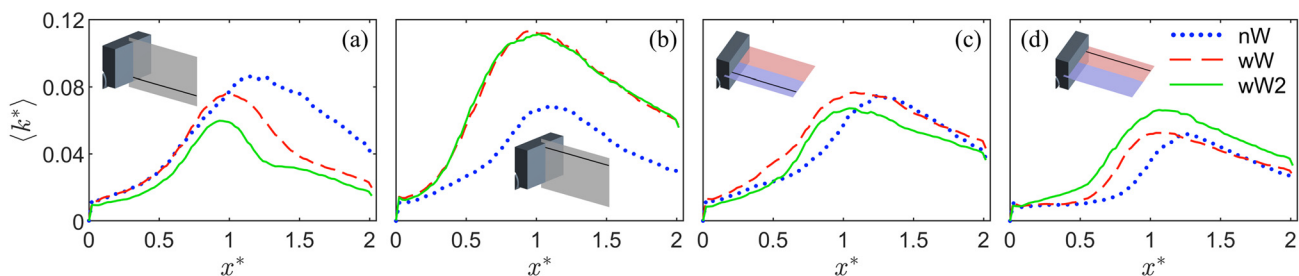
FIG. 16. Distributions of turbulent kinetic energy along lines at $z^* = 0.27$ (a) and 1.07 (b) in the vertical plane of symmetry and $x^* = -0.5$ (c) and 0.5 (d) in the mid-height plane.

~45% larger than that on the right line in the state R for cases nW and wW due to the asymmetric wake dynamics.

D. The coherent dynamics of the wake

The wake dynamics is further investigated with the aim of paving the way for the development of efficient flow control strategies for road vehicles. A low-order model (LOM) based on proper orthogonal decomposition (POD), which has been widely used for flow analysis and control (Rowley and Dawson, 2017; Pavia et al., 2020; Plumejeau et al., 2020; Fan et al., 2020; and Podvin et al., 2021), was applied to reveal the dominant motions. A brief derivation of the LOM is shown as follows. First, the flow snapshot $\chi(\boldsymbol{x}, t)$ at position $\boldsymbol{x}$ is decomposed into the mean field $\overline{\chi}(\boldsymbol{x})$, and the fluctuating part $\chi'(\boldsymbol{x}, t)$, as

$$\chi(\boldsymbol{x}, t) = \overline{\chi}(\boldsymbol{x}) + \chi'(\boldsymbol{x}, t). \tag{1}$$

The fluctuating part is then approximated by the Singular Value Decomposition (SVD) approach with spatially dependent modes $\phi_i(\boldsymbol{x})$ and the corresponding temporal coefficients $a_i(t)$,

$$\chi'(\boldsymbol{x}, t) = \sum_{i=1}^{N} \phi_i(\boldsymbol{x}) a_i(t). \tag{2}$$

For an ensemble of n time-discrete snapshots recorded at m spatial points, the number of POD modes N is limited to $\min\{m, n\}$. The SVD approach returns singular values in descending order, which allows the POD modes to be ranked by the energy content of each mode. The energy content of a single mode $K_i(t)$ is given by

$$K_i(t) = \frac{1}{2} a_i^2(t), \tag{3}$$

and the total fluctuation energy $K_\Sigma(t)$ is evaluated as

$$K_\Sigma(t) = \sum_{i=1}^{N} K_i(t). \tag{4}$$

Thus, using a limited number of POD modes allows to concentrate the main dynamic features. The flow field reconstructed by the LOM is

$$\chi_{LOM}(\boldsymbol{x}, t) = \overline{\chi}(\boldsymbol{x}) + \sum_{i=1}^{M} \phi_i(\boldsymbol{x}) a_i(t), \tag{5}$$

with $M < N$. More information concerning the application of such a technique to fluid dynamic investigations is provided in Zhou et al. (2021).

In the present study, the POD is applied on snapshots of velocity components $[u^*(x, y, t), v^*(x, y, t)]$ and pressure coefficient $C_p(x, y, t)$. The snapshots are obtained with a constant time step (25 t_c) over $x^* \in [-0.13, 2.00]$ and $y^* \in [-0.76, 0.76]$ in the $z^* = 0.67$ plane. Note that for the velocity field, the streamwise and spanwise velocity fluctuations are concatenated into the same snapshot matrix to compute the POD. Figures 17(a) and 17(b) show the energy contribution of the first 100 velocity and pressure modes. The energy proportion beyond the 50th mode is less than 0.4%, and a large chunk of the total fluctuation energy is well represented by the first 50 modes (above 45% and 60% for the velocity and pressure modes, respectively). Hence, the first 50 energetic POD modes are used to reconstruct the low-order flow organizations, which are well representative of the sub-scale turbulence and sufficient to identify the main coherent structures, as visualized in Fig. 17(c).

Figures 18–20 (Multimedia views) show the unsteady evolution of the near wake in the preferred asymmetric or symmetric state for the three cases, respectively. In order to focus on wake oscillation features induced by lateral shear layer interactions, four consecutive time instants in one typical shedding cycle with a period $T_s^* \approx 7$ are
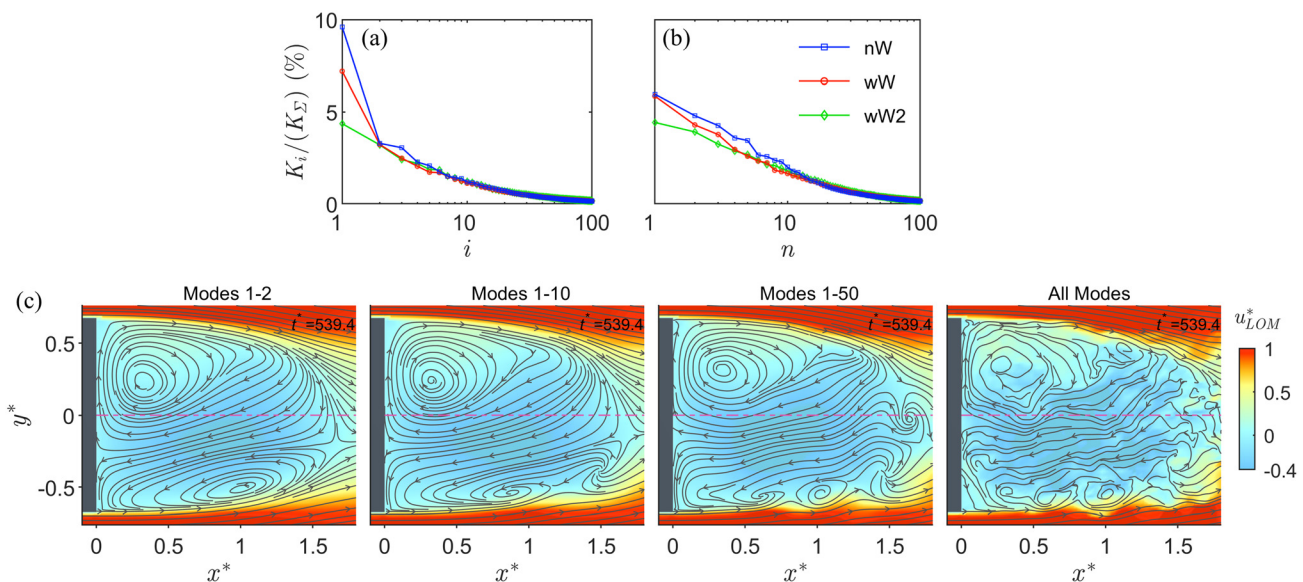
FIG. 17. Energy contribution of POD modes 1–100. POD analysis is applied to (a) the velocity field and (b) pressure field in the $z^* = 0.67$ plane. (c) Comparison of a low-order velocity field built by different number of modes.
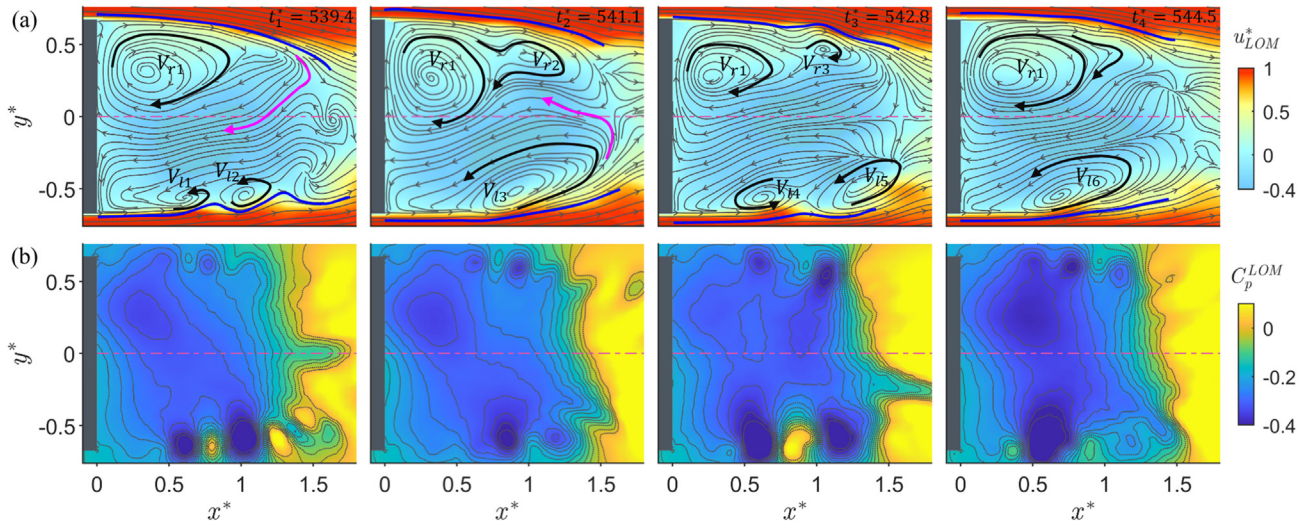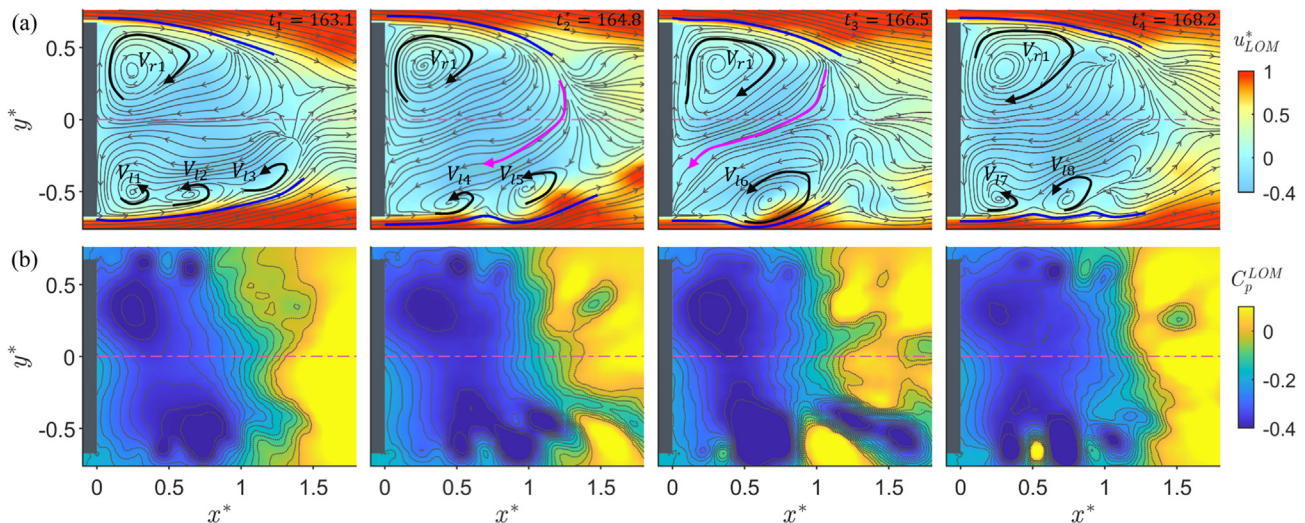
FIG. 18. Evolution of the low-order velocity field (a) and corresponding pressure field (b) in the $z^* = 0.67$ plane for case nW. The time between successive instants is $225\Delta t^*$ (around 1/4 of the vortex shedding cycle). In (a), black lines represent recirculation flow, blue lines represent shear layers, and magenta lines represent flow transfer. Multimedia view: https://doi.org/10.1063/5.0138305.1

selected to characterize the evolution in detail. It is important to note that the phases of the four selected instances do not match in different cases. Nevertheless, phase matching is not considered necessary here because the comparison of the three cases is to show different patterns of the main flow dynamics not the differences at specific phases. Due to the high occurrence of the selected instances in the set of flow snapshots, the exhibited behavior can be considered significant.

For case nW (Fig. 18), convective co-rotating vortices V_{l1} and V_{l2} on the inner side of the left shear layer and a co-flow V_{r1} on the inner side of the right shear layer are observed at t_1^*. The right co-flow bubble is much bigger in size, and certain airflow is transported to the left

region. At t_2^*, a vortex V_{r2} sheds from the V_{r1} on the right, while the left vortices merge into a large one V_{l3} with certain flow moving to the right. At t_3^*, the right bubble V_{r1} starts its growth in size, and the separated structure V_{r3} vanishes rapidly, while the left bubble V_{l3} collapses into two co-rotating vortices V_{l4} and V_{l5}. At t_4^*, the right bubble V_{r1} starts to release structures again, and the left vortices merge back into a large bubble V_{l6}. Unlike the low-pressure region tilted away from the left base at t_1^* and t_2^* [Fig. 18(b)], the pressure between left and right regions is distributed toward equilibrium at t_3^* and t_4^*. Nevertheless, the asymmetry is maintained into the next shedding cycle, repeating the evolution of t_1^* to t_4^* until the wake reversal to the other

FIG. 19. Evolution of the low-order velocity field (a) and corresponding pressure field (b) in the $z^* = 0.67$ plane for case wW. The time between successive instants is $225\Delta t^*$ (around 1/4 of the vortex shedding cycle). Multimedia view: https://doi.org/10.1063/5.0138305.2
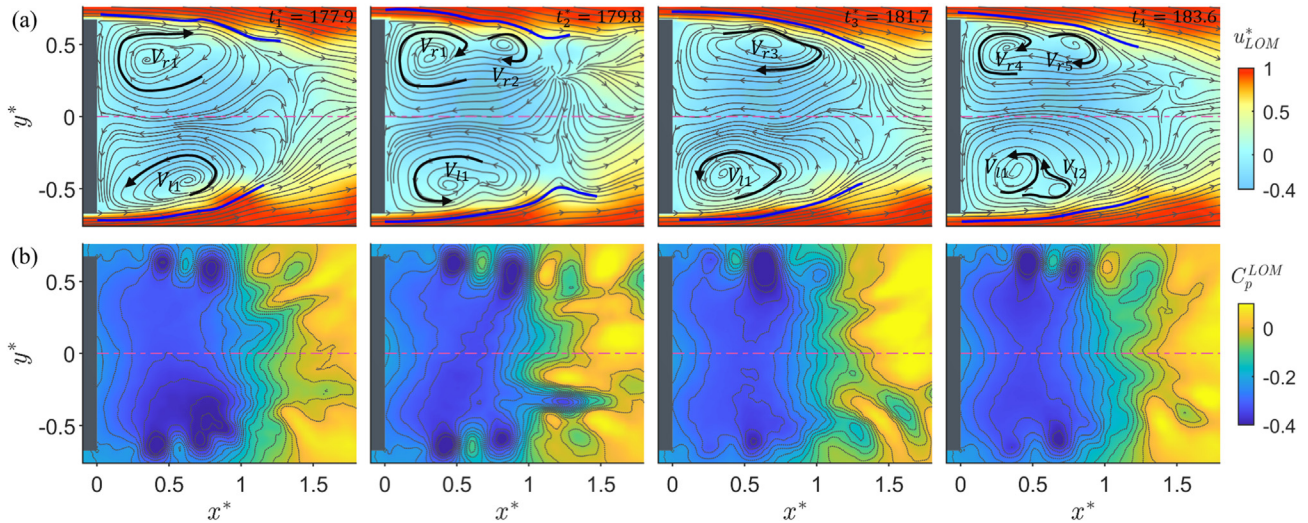
FIG. 20. Evolution of the low-order velocity field (a) and corresponding pressure field (b) in the $z^* = 0.67$ plane for case wW2. The time between successive instants is $250\Delta t^*$ (around 1/4 of the vortex shedding cycle). Multimedia view: https://doi.org/10.1063/5.0138305.3

asymmetric state. These repetitive phenomena clearly show the coherent dynamics at left and right downstream the base.

For case wW (Fig. 19), the behavior of the vortex loops emanating from the left side of the wake is quite in line with that shown in case nW, where vortex bursts and merges occur alternately. The obvious difference is on the right, in which the large bubble rarely releases coherent structures; instead, fluid is entrained into the left recirculation region (as indicated at t_2^* and t_3^*). Also discernible is a decrease in pressure within the right bubble. These alterations are a direct consequence of the increase in the curvature of the right shear layer (sketched in blue), which has a stabilizing effect on the shear layer (Liou, 1994). It can be inferred that the reduced flow rate yielded by the addition of the wheels enhances entrainment not only at the bottom but also at the side shear layers. A more stable organization on one side of the asymmetric state explains why the wheels could strengthen the bi-stable mode in current case.

For case wW2 (Fig. 20), co-flow occurs on the inner side of both side shear layers and the lateral asymmetry of pressure virtually vanishes. This can be explained by the fact that the further upwash flow stabilizes the lateral shear layers resulting in amplified shedding structures. The large-scale structures consequently enhance mixing and energy transfer in the wake.

In summary, the shear layer on one side of the wake bends toward the recirculation region, while the shear layer on the opposite side leading to the vortex roll-up is more aligned with the free-stream in the asymmetric state for cases nW and wW. This feature is also reported in the literature for bi-stable wakes of Ahmed body (Haffner et al., 2020; Plumejeau et al., 2020), whereas for case wW2, highly curved recirculating bubbles are formed on both sides of the wake.

Complementary spectral analysis would help in clarifying the dominant dynamics. In Fig. 21, the spectrum of streamwise velocity fluctuations at the locations indicated by circles in lateral shear layers
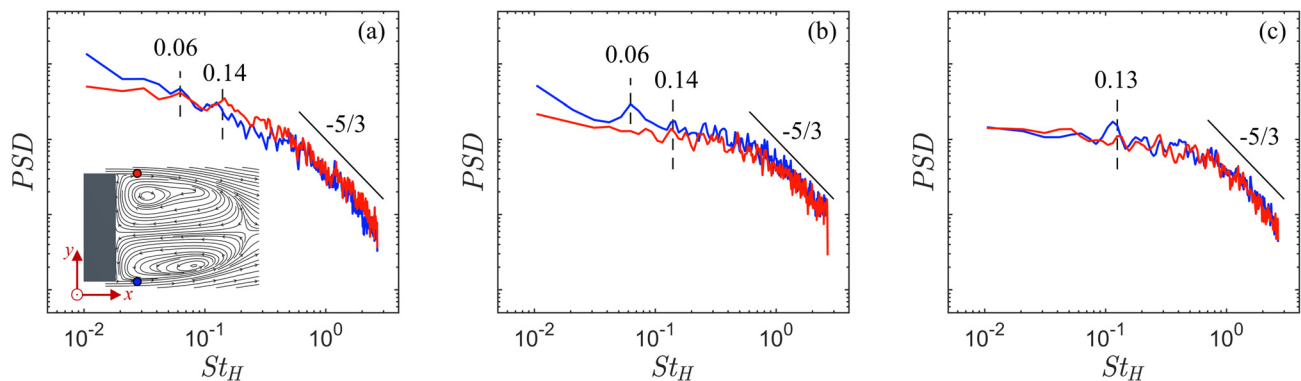
FIG. 21. Power spectra density of the streamwise velocity fluctuations at a point in each side shear layer in the $z^* = 0.67$ plane for case nW (a), case wW (b), and case wW2 (c).
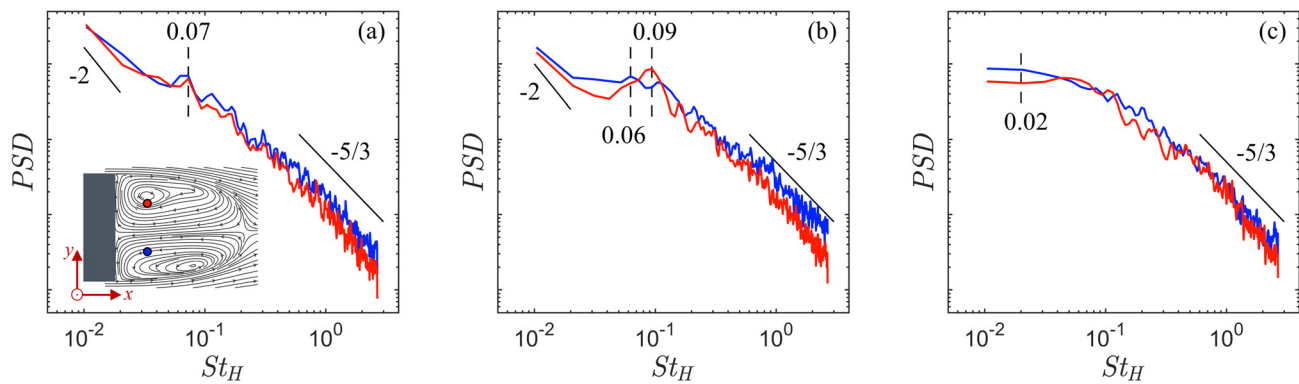
FIG. 22. Power spectra density of the streamwise velocity fluctuations at a point in each recirculation bubble in the $z^* = 0.67$ plane for case nW (a), case wW (b), and case wW2 (c).

is presented. Note that cases nW and wW have a predominance of the state R in the current simulation time. A peak at $St_H \sim 0.13$ is seen in all three cases and is related to the vortex shedding mode in the horizontal plane. A second peak at $St_H \sim 0.06$ associated with the bubble-pumping mode (Volpe *et al.*, 2015; Pavia *et al.*, 2017) appears in both side shear layers of case nW and in the left shear layer of case wW, but not in case wW2. This is consistent with the previous discussion that lateral shear layers are stabilized by the upwash flow and exhibit rather static behavior than quasi-periodic shrinking and expansion. Differences are also observed in the lower frequency range. In cases nW and wW, dominated by the state R, the left shear layer is significantly more energetic than the right one at $St_H < 0.04$. By contrast, in case wW, the two have almost equal energy levels. In addition, a distribution of energy almost proportional to the $-5/3$ power law at $St_H > 0.6$ is observed in all three cases, as expected by the Kolmogorov theory.

Figure 22 illustrates the spectrum of velocity fluctuations inside the recirculation region. The pumping motion with $St_H \sim 0.07$ is again confirmed in the whole recirculating region of case nW and in the left wake of case wW. The peak at $St_H \sim 0.09$ in the right wake of case wW was interpreted by Pavia (2019) as a localized flapping motion. The -2 law decay at very low frequencies is observed on both sides of the wake for cases nW and wW, suggesting that the bi-stable mode involves the interaction of all the recirculating flow. In case wW2, the long-time bi-stable dynamics is replaced by a swinging motion named by Pavia (2019), as evidenced by the inflection point observed at $St_H \sim 0.02$.

IV. CONCLUSIONS

This numerical study analyzed the flow characteristics around a squareback bluff-body with and without wheels, which will assist in future development of efficient flow control strategies for more realistic vehicles. The second aim of this study was to clarify the controversial experimental findings on whether bi-stable behavior persists when wheels are applied to the simplified automotive geometry. After validating the accuracy of the numerical setup of IDDES, three cases were examined at $Re = 0.96 \times 10^5$: the squareback Windsor body without wheels encountering a uniform inflow (case nW), the squareback Windsor model with wheels in uniform inflow (case wW), and immersed in a thick boundary layer, $\delta_{99} = 1.3C$ (case wW2). The major conclusions are summarized below:

- The underbody flow rate is a key factor in altering the dynamic behavior of the wake, as the underbody flow with diminished momentum is not able to maintain its advection close to the ground and is entrained to the recirculation region.
- When wheels are equipped, the underbody flow rate is reduced by 22%, and a downwash dominated wake switches to an upwash dominated wake. The upwash effect makes the base impingement point move up and recovers pressure on the upper portion of the base, forming a "U" shaped pressure distribution. The upwash effect also reduces the volume of recirculation zone by over 16% and brings the vortex cores much closer to the base, resulting in a 9% increase in base suction. Moreover, the Reynolds stresses in the bottom shear layer are damped but considerably enhanced in the upper shear layer.
- Long-term bi-stable behavior is detected only in cases nW and wW. For case wW2, the bi-stability largely disappears, which reproduces the finding of Pavia *et al.* (2020). However, considering the uniform inflow (ideal road condition), case wW reinforces the finding of Grandemange *et al.* (2013a) that the bi-stability exists for realistic vehicles with wheels. This suggests that the removal of bi-stability is the result of a further strengthening of the interaction between the wake recirculation and the bottom flow due to the thick oncoming floor boundary layer, which settles the conflict in previous findings.
- The coupling of dominant wake dynamics was exhibited by utilizing low-order modeling to elaborate the evolution of coherent structures. For a given asymmetric state in cases nW and wW, the shear layer on one side of the wake bends toward the recirculation region, while the shear layer on the opposite side leading to the vortex roll-up remains more aligned with the free-stream. Case wW has one shear layer with increased curvature, and as such, it is stabilized. The more stable structure explains why the wheels could strengthen the bi-stable mode in case wW, whereas for case wW2, highly curved recirculating flows are formed on both sides of the wake due to the high degree of interaction in the wake.
- The dominant wake dynamics was distinguished by spectral analysis. The wake vortex shedding mode at $St_H \sim 0.13$ is seen in the lateral shear layers for all three cases. The bubble-pumping mode at $St_H \sim 0.06$ appears in the whole wake in case nW and

only the unstable side of wake in case wW, but not in case wW2. The -2 law decay at very low frequencies linked to the bi-stable mode involves the interaction of all the recirculating flow for cases nW and wW. Instead, an inflection point is observed at $St_H \sim 0.02$ in case wW2 and is related to a swinging motion of the rear recirculation.

ACKNOWLEDGMENTS

AUTHOR DECLARATIONS

Conflict of Interest

The authors have no conflicts to disclose.

Author Contributions

Xinchao Su: Conceptualization (equal); Formal analysis (equal); Investigation (equal); Methodology (equal); Software (equal); Validation (equal); Visualization (equal); Writing – original draft (equal); Writing – review & editing (equal). **Kan He:** Formal analysis (supporting); Writing – review & editing (supporting). **Kewei Xu:** Formal analysis (supporting); Investigation (supporting); Writing – review & editing (equal). **Guangjun Gao:** Funding acquisition (equal); Project administration (equal); Supervision (equal). **Sinisa Krajnović:** Funding acquisition (equal); Project administration (equal); Resources (equal); Supervision (equal); Writing – review & editing (equal).

DATA AVAILABILITY

The data that support the findings of this study are available from the corresponding author upon reasonable request.

REFERENCES

Ahmed, S. R., Ramm, G., and Faltin, G., "Some salient features of the time-averaged ground vehicle wake," in *SAE Transactions* (SAE International, 1984), pp. 473–503.

Aleyasin, S. S., Tachie, M. F., and Balachandar, R., "Characteristics of flow past elongated bluff bodies with underbody gaps due to varying inflow turbulence," Phys. Fluids **33**(12), 125106 (2021).

Aljure, D. E., Calafell, J., Baez, A., and Oliva, A., "Flow over a realistic car model: Wall modeled large eddy simulations assessment and unsteady effects," J. Wind Eng. Ind. Aerodyn. **174**, 225–240 (2018).

Bao, D., Borée, J., Haffner, Y., and Sicot, C., "Near wake interactions and drag increase regimes for a square-back bluff body," J. Fluid Mech. **936**, A2 (2022).

Barros, D., Borée, J., Noack, B. R., Spohn, A., and Ruiz, T., "Bluff body drag manipulation using pulsed jets and Coanda effect," J. Fluid Mech. **805**, 422–459 (2016).

Beaudoin, J. F., and Aider, J. L., "Drag and lift reduction of a 3D bluff body using flaps," Exp. Fluids **44**(4), 491–501 (2008).

Brackston, R. D., García de la Cruz, J. M., Wynn, A., Rigas, G., and Morrison, J. F., "Stochastic modelling and feedback control of bistability in a turbulent bluff body wake," J. Fluid Mech. **802**, 726–749 (2016).

Buchheim, R., Deutenbach, K. R., and Lückoff, H. J., "Necessity and premises for reducing the aerodynamic drag of future passenger cars," in *SAE Transactions* (SAE International, 1981), pp. 758–771.

Burton, D., Wang, S., Smith, D. T., Scott, H. N., Crouch, T. N., and Thompson, M. C., "The influence of background turbulence on Ahmed-body wake bistability," J. Fluid Mech. **926**, R1 (2021).

Cadot, O., "Stochastic fluid structure interaction of three-dimensional plates facing a uniform flow," J. Fluid Mech. **794**, R1 (2016).

Cadot, O., Evrard, A., and Pastur, L., "Imperfect supercritical bifurcation in a three-dimensional turbulent wake," Phys. Rev. E **91**(6), 063005 (2015).

Cebeci, T., "General behavior of turbulent boundary layers," in *Analysis of Turbulent Flows with Computer Programs* (Butterworth-Heinemann, 2013), pp. 89–153.

Choi, H., Lee, J., and Park, H., "Aerodynamics of heavy vehicles," Annu. Rev. Fluid Mech. **46**(1), 441–468 (2014).

Dalla Longa, L., Evstafyeva, O., and Morgans, A. S., "Simulations of the bi-modal wake past three-dimensional blunt bluff bodies," J. Fluid Mech. **866**, 791–809 (2019).

Evrard, A., Cadot, O., Herbert, V., Ricot, D., Vigneron, R., and Délery, J., "Fluid force and symmetry breaking modes of a 3D bluff body with a base cavity," J. Fluids Struct. **61**, 99–114 (2016).

Fan, Y., Xia, C., Chu, S., Yang, Z., and Cadot, O., "Experimental and numerical analysis of the bi-stable turbulent wake of a rectangular flat-backed bluff body," Phys. Fluids **32**(10), 105111 (2020).

Gilliéron, P., and Kourta, A., "Aerodynamic drag control by pulsed jets on simplified car geometry," Exp. Fluids **54**(2), 1457 (2013).

Grandemange, M., Cadot, O., Courbois, A., Herbert, V., Ricot, D., Ruiz, T., and Vigneron, R., "A study of wake effects on the drag of Ahmed's squareback model at the industrial scale," J. Wind Eng. Ind. Aerodyn. **145**, 282–291 (2015).

Grandemange, M., Gohlke, M., and Cadot, O., "Turbulent wake past a three-dimensional blunt body. I. Global modes and bi-stability," J. Fluid Mech. **722**, 51–84 (2013a).

Grandemange, M., Gohlke, M., and Cadot, O., "Bi-stability in the turbulent wake past parallelepiped bodies with various aspect ratios and wall effects," Phys. Fluids **25**(9), 095103 (2013b).

Grandemange, M., Gohlke, M., and Cadot, O., "Turbulent wake past a three-dimensional blunt body. II. Experimental sensitivity analysis," J. Fluid Mech. **752**, 439–461 (2014).

Gritskevich, M. S., Garbaruk, A. V., Schütze, J., and Menter, F. R., "Development of DDES and IDDES Formulations for the k-ω shear stress transport model," Flow, Turbul. Combust. **88**(3), 431–449 (2012).

Gulyás, A., Bodor, Á., Regert, T., and Jánosi, I. M., "PIV measurement of the flow past a generic car body with wheels at LES applicable Reynolds number," Int. J. Heat Fluid Flow **43**, 220–232 (2013).

Haffner, Y., Borée, J., Spohn, A., and Castelain, T., "Mechanics of bluff body drag reduction during transient near-wake reversals," J. Fluid Mech. **894**, A14 (2020).

He, K., Minelli, G., Su, X., Gao, G., and Krajnović, S., "Influence of the rounded rear edge on wake bi-stability of a notchback bluff body," Phys. Fluids **33**(11), 115107 (2021a).

He, K., Minelli, G., Su, X., Gao, G., and Krajnović, S., "On state instability of the bi-stable flow past a notchback bluff body," J. Fluid Mech. **931**, R6 (2022).

He, K., Minelli, G., Wang, J., Gao, G., and Krajnović, S., "Assessment of LES, IDDES and RANS approaches for prediction of wakes behind notchback road vehicles," J. Wind Eng. Ind. Aerodyn. **217**, 104737 (2021b).

Hesse, F. and Morgans, A. S., "Simulation of wake bimodality behind squareback bluff-bodies using LES," Comput. Fluids **223**, 104901 (2021).

Hucho, W. H., Janssen, L. J., and Schwartz, G., "The wind tunnel's ground plane boundary layer: Its interference with the flow underneath cars," in *SAE Transactions* (SAE International, 1975), pp. 380–389.

Huminic, A. and Huminic, G., "Aerodynamic study of a generic car model with wheels and underbody diffuser," Int. J. Automot. Technol. **18**(3), 397–404 (2017).

Jeong, J. and Hussain, F., "On the identification of a vortex," J. Fluid Mech. **285**, 69–94 (1995).

Kang, N., Essel, E. E., Roussinova, V., and Balachandar, R., "Effects of approach flow conditions on the unsteady three-dimensional wake structure of a square-back Ahmed body," Phys. Rev. Fluids **6**(3), 034613 (2021).

Kohri, I., Yamanashi, T., Nasu, T., Hashizume, Y., and Katoh, D., "Study on the transient behaviour of the vortex structure behind Ahmed body," SAE Int. J. Passenger Cars: Mech. Syst. **7**(2), 586–602 (2014).

Krajnović, S., "Large eddy simulation exploration of passive flow control around an Ahmed body," J. Fluids Eng. **136**(12), 121103 (2014).

Krajnović, S. and Davidson, L., "Numerical study of the flow around a bus-shaped body," J. Fluids Eng. **125**(3), 500–509 (2003).

Krajnović, S. and Davidson, L., "Flow around a simplified car. II. Understanding the flow," J. Fluids Eng. **127**(5), 919–928 (2005).

Le Good, G. M. and Garry, K. P., "On the use of reference models in automotive aerodynamics," SAE Technical Report No. 2004-01-1308, 2004.

Li, R., Barros, D., Borée, J., Cadot, O., Noack, B. R., and Cordier, L., "Feedback control of bimodal wake dynamics," Exp. Fluids **57**(10), 158 (2016).

Liou, W. W., "Linear instability of curved free shear layers," Phys. Fluids **6**(2), 541–549 (1994).

Liu, K., Zhang, B. F., Zhang, Y. C., and Zhou, Y., "Flow structure around a low-drag Ahmed body," J. Fluid Mech. **913**, A21 (2021).

Lorite-Díez, M., Jiménez-González, J. I., Pastur, L., Martínez-Bazán, C., and Cadot, O., "Experimental analysis of the effect of local base blowing on three-dimensional wake modes," J. Fluid Mech. **883**, A53 (2020).

Lucas, J. M., Cadot, O., Herbert, V., Parpais, S., and Délery, J., "A numerical investigation of the asymmetric wake mode of a squareback Ahmed body: Effect of a base cavity," J. Fluid Mech. **831**, 675–697 (2017).

Minelli, G., Tokarev, M., Zhang, J., Liu, T., Chernoray, V., Basara, B., and Krajnović, S., "Active aerodynamic control of a separated flow using streamwise synthetic jets," Flow, Turbul. Combust. **103**(4), 1039–1055 (2019).

Pavia, G., Passmore, M. A., Varney, M., and Hodgson, G., "Salient three-dimensional features of the turbulent wake of a simplified square-back vehicle," J. Fluid Mech. **888**, A33 (2020).

Pavia, G., "Characterisation of the unsteady wake of a square-back road vehicle," Ph.D. thesis (Loughborough University, 2019).

Pavia, G., Passmore, M., and Sardu, C., "Evolution of the bi-stable wake of a square-back automotive shape," Exp. Fluids **59**(1), 20 (2018).

Perry, A.-K., Pavia, G., and Passmore, M., "Influence of short rear end tapers on the wake of a simplified square-back vehicle: Wake topology and rear drag," Exp. Fluids **57**(11), 169 (2016).

Plumejeau, B., Delprat, S., and Keirsbulck, L., "Ultra-local model-based control of the square-back Ahmed body wake flow," Phys. Fluids **31**(8), 085103 (2019).

Plumejeau, B., Keirsbulck, L., Delprat, S., Lippert, M., and Abassi, W., "Behavior of the square-back Ahmed body global modes at low ground clearance," Phys. Rev. Fluids **5**(8), 084701 (2020).

Podvin, B., Pellerin, S., Fraigneau, Y., Bonnavion, G., and Cadot, O., "Low-order modelling of the wake dynamics of an Ahmed body," J. Fluid Mech. **927**, R6 (2021).

Pujals, G., Depardon, S., and Cossu, C., "Drag reduction of a 3D bluff body using coherent streamwise streaks," Exp. Fluids **49**(5), 1085–1094 (2010).

Rao, A., Minelli, G., Basara, B., and Krajnović, S., "On the two flow states in the wake of a hatchback Ahmed body," J. Wind Eng. Ind. Aerodyn. **173**, 262–278 (2018).

Rejniak, A. A. and Gatto, A., "Influence of rotating wheels and moving ground use on the unsteady wake of a small-scale road vehicle," Flow, Turbul. Combust. **106**(1), 109–137 (2021).

Rowley, C. W. and Dawson, S. T. M., "Model reduction for flow analysis and control," Annu. Rev. Fluid Mech. **49**(1), 387–417 (2017).

Schuetz, T., *Aerodynamics of Road Vehicles*, 5th ed. (SAE International, 2015).

Thacker, A., Aubrun, S., Leroy, A., and Devinant, P., "Effects of suppressing the 3D separation on the rear slant on the flow structures around an Ahmed body," J. Wind Eng. Ind. Aerodyn. **107108**, 237–243 (2012).

Urquhart, M., Varney, M., Sebben, S., and Passmore, M., "Aerodynamic drag improvements on a square-back vehicle at yaw using a tapered cavity and asymmetric flaps," Int. J. Heat Fluid Flow **86**, 108737 (2020).

Varney, M., "Base drag reduction for squareback road vehicles," Ph.D. thesis (Loughborough University, 2020).

Varney, M., Pavia, G., Passmore, M., and Crickmore, C. (2020). "Windsor model experimental aerodynamic dataset," Loughborough University, https://doi.org/10.17028/rd.lboro.13161284

Veerasamy, D., Tajik, A. R., Pastur, L., and Parezanović, V., "Effect of base blowing by a large-scale fluidic oscillator on the bistable wake behind a flat-back Ahmed body," Phys. Fluids **34**(3), 035115 (2022).

Venning, J., Lo Jacono, D., Burton, D., Thompson, M. C., and Sheridan, J., "The nature of the vortical structures in the near wake of the Ahmed body," Proc. Inst. Mech. Eng., Part D **231**(9), 1239–1244 (2017).

Volpe, R., Devinant, P., and Kourta, A., "Experimental characterization of the unsteady natural wake of the full-scale square back Ahmed body: Flow bi-stability and spectral analysis," Exp. Fluids **56**(5), 99 (2015).

Wang, Y., Sicot, C., Borée, J., and Grandemange, M., "Experimental study of wheel-vehicle aerodynamic interactions," J. Wind Eng. Ind. Aerodyn. **198**, 104062 (2020).

Wäschle, A., "The influence of rotating wheels on vehicle aerodynamics: Numerical and experimental investigations," SAE Technical Report No. 2007-01-0107 (2007).

Wood, A., Passmore, M., Forbes, D., Wood, D., and Gaylard, A., "Base pressure and flow-field measurements on a generic SUV model," SAE Int. J. Passenger Cars: Mech. Syst. **8**(1), 233–241 (2015).

Xu, K., Su, X., Bensow, R., and Krajnovic, S., "Drag reduction of ship airflow using steady Coanda effect," Ocean Eng. **266**, 113051 (2022).

Xu, K., Su, X., Bensow, R., and Krajnovic, S., "Large eddy simulation of ship airflow control with steady Coanda effect," Phys. Fluids **35**(1), 015112 (2023).

Zhang, B. F., Zhou, Y., and To, S., "Unsteady flow structures around a high-drag Ahmed body," J. Fluid Mech. **777**, 291–326 (2015).

Zhou, L., Tse, K. T., Hu, G., and Li, Y., "Mode interpretation of interference effects between tall buildings in tandem and side-by-side arrangement with POD and ICA," Eng. Struct. **243**, 112616 (2021).

Zhou, L., Zhang, Z., Zhang, B., and Tse, K. T., "Receptivity-orientated drag reduction of twin cylinders by steady leading-edge suction control based on adjoint method," Phys. Fluids **34**(12), 123605 (2022).